

<https://doi.org/10.1038/s42003-024-07302-2>

Spatiotemporal modeling quantifies cellular contributions to uptake of *Aspergillus fumigatus* in the human lung



Christoph Saffer^{1,2}, Sandra Timme¹, Sébastien C. Ortiz³, Margherita Bertuzzi³ & Marc Thilo Figge^{1,4}

The human lung is confronted daily with thousands of microbial invaders reaching the lower respiratory tract. An efficient response by the resident type 1 and type 2 alveolar epithelial cells (AECs) and alveolar macrophages (AMs) cells during the early hours of innate immunity is a prerequisite to maintain a non-inflammatory state, but foremost to rapidly remove harmful substances. One such human-pathogenic invader is the opportunistic fungus *Aspergillus fumigatus*. If the spherical conidia are not cleared in time, they swell reaching approximately twice of their initial size and germinate to develop hyphae around six hours post-infection. This process of morphological change is crucial as it enables the pathogen to invade the alveolar epithelium and to reach the bloodstream, but also makes it conspicuous for the immune system. During this process, conidia are first in contact with AECs then with migrating AMs, both attempting to internalize and clear the fungus. However, the relative contribution of AMs and AECs to uptake of *A. fumigatus* remains an open question, especially the capabilities of the barely investigated type 1 AECs. In this study, we present a bottom-up modeling approach to incorporate experimental data on the dynamic increase of the conidial diameter and *A. fumigatus* uptake by AECs and AMs in a hybrid agent-based model (hABM) for the to-scale simulation of virtual infection scenarios in the human alveolus. By screening a wide range of parameters, we found that type 1 AECs, which cover approximately 95% of the alveolar surface, are likely to have a greater impact on uptake than type 2 AECs. Moreover, the majority of infection scenarios across the regime of tested parameters were cleared through uptake by AMs, whereas the contribution to conidial uptake by AECs was observed to be limited, indicating that their crucial support might mostly consist in mediating chemokine secretion for AM recruitment. Regardless, as the first host cell being confronted with *A. fumigatus* conidia, our results evidence the large potential impact of type 1 AECs antimicrobial activities, underlining the requirement of increasing experimental efforts on this alveolar constituent.

The innate immune system constitutes the first line of defense in the protection of the human body against invading microbes. Due to the continuous inhalation of particles by humans, the immune system is permanently challenged to rapidly remove harmful microbes from the lungs to maintain a non-inflammatory and healthy state¹. Alveolar epithelial cells (AECs) line the lung alveoli and thus act as a physical barrier to noxious particles, making them important players in immune defense by preventing

microbes from entering the bloodstream^{2,3}. The relatively large and flat type 1 AECs make up about 95% of the alveolar surface^{4,5}, although they are outnumbered by the smaller surfactant-producing type 2 AECs that cover only about 5%⁶. Inhaled microbes reaching the lower respiratory tract encounter AECs that – besides functioning as physical barriers – are also able to internalize and kill invading microbes^{7–9}. In addition, AECs secrete cytokines and chemokines that may recruit alveolar macrophages (AMs),

¹Research Group Applied Systems Biology, Leibniz Institute for Natural Product Research and Infection Biology – Hans Knöll Institute, Jena, Germany. ²Faculty of Biological Sciences, Friedrich Schiller University Jena, Jena, Germany. ³Manchester Fungal Infection Group, Faculty of Biology, Medicine and Health, The University of Manchester, Core Technology Facility, Manchester, UK. ⁴Institute of Microbiology, Faculty of Biological Sciences, Friedrich Schiller University Jena, Jena, Germany. ✉e-mail: thilo.figge@leibniz-hki.de

which are the professional phagocytes resident in lung alveoli^{8,10,11}. AMs patrol the alveolar surface in numbers that vary dynamically around twelve cells per alveolus^{12,13} to detect and clear harmful particles within hours post-infection^{14–16}. However, it is still not understood what the relative contribution of AMs and AECs is in the uptake of particles to prevent respiratory diseases^{17,18}.

One such respiratory threat is due to the ubiquitous mold *Aspergillus fumigatus*^{19,20}. This opportunistic pathogen is often diagnosed too late and – since treatment options are limited – is associated with mortality rates up to 90% in immunocompromised patients^{19,21,22}. Consequently, *A. fumigatus* is one of four human-pathogenic fungi that belong to the Critical Priority Group according to the recently updated rating by the World Health Organization (WHO)^{23–25}. Humans inhale several hundred *A. fumigatus* conidia per day²⁶ and these, due to their small size ($\sim 2\text{--}3\ \mu\text{m}$ diameter), reach the alveoli in the lower respiratory tract^{20,27}. If able to evade the innate immune response, conidia pose a substantial risk for immunocompromised patients^{28,29}. Due to the large number of alveoli in the human lung (~ 500 million), no more than one conidium per alveolus can be expected on statistical grounds^{13,30}. The spherical conidium will adhere to AECs and, after roughly two hours, will start to swell reaching up to twice its initial diameter³¹. At around six hours post-infection, germination of the conidium begins with the formation of hyphae, which are able to damage the alveolar epithelium and penetrate the lung tissue to enter blood vessels leading to clotting or dissemination via the bloodstream^{32,33}. The innate immune response to inhaled *A. fumigatus* conidia is mediated by both AECs and AMs³⁴ via recognition, uptake, and clearance of their internalized cargoes^{35–40}, but the relative contribution of these cells to conidial removal from the alveolus in the early hours is a subject of ongoing discussions⁴¹. In addition, the differences between type 1 and type 2 AECs in terms of their phagocytic capabilities are barely explored, as the experimental data on type 1 AECs is sparse because of their difficult cell cultivation and rare established in vitro protocols⁴².

Understanding the underlying mechanisms of the complex interplay between *A. fumigatus* conidia and the early innate immune system is crucial to improving diagnosis and treatment. To investigate this, wet-lab experiments can be combined with mathematical analyses representing the heart of systems biology^{43,44}. In this multidisciplinary approach, computational models are used to simulate complex biological systems that are calibrated to experimental data allowing millions of virtual experiments to be conducted⁴⁵. The mathematical description of systems can be realized by ordinary differential equations (ODEs) or partial differential equations (PDEs), state-based models or agent-based models, and game theory^{46–50,45,51–54}. Agent-based models are computationally expensive but can account for stochastic systems with inhomogeneous properties, e.g., to investigate microbial infections in whole-blood^{55,56} or modeling receptor-ligand binding kinetics at the single cell level⁵⁷. In the past, we developed a hybrid agent-based model of a human alveolus (hABM), which was applied in earlier studies to explore the impact of AM numbers¹³, investigate the function of pores of Kohn⁵⁸, compare the immune response in the murine and human alveoli³⁰, as well as quantify the impact of chemokine secretion on fungal clearance^{59,60}.

In the present study, we investigated the early immune response against *A. fumigatus* in the human lung and, specifically how type 1 and type 2 AECs and AMs contribute to fungal clearance. Based on newly evaluated experimental data from Bertuzzi et al.^{35,36} and in line with previous experimental findings^{37,61,62} indicating a more efficient uptake of swollen conidia, we developed a conidial growth model linking conidial uptake by AECs and AMs to conidial swelling and integrated it into the previously developed hABM^{13,30,58–60}. We ran millions of stochastic computer simulations and predicted the *A. fumigatus* uptake contributions by type 1 and type 2 AECs and AMs during the first hours post-infection. Assuming that conidial swelling also determines the pathogen recognition as such and the subsequent onset of chemokine secretion by AECs, we investigated fungal clearance for shifted onsets of chemokine secretion. Also, we screened over reduced and increased AM numbers simulating compromised and primed early immune states. Our simulations suggest that, in the majority of

infection scenarios, fungal clearance is dominated by phagocytosis due to AMs, while uptake by AECs decisively depends on whether the conidium is confronted with type 1 or type 2 AECs. To analyze the large amount of simulation outcomes further, we fitted a surrogate infection model¹³ enabling the prediction of requisite uptake rates of host cells for timely fungal clearance. In summary, we present a bottom-up modeling approach based on experimental data that links conidial swelling to its recognition and uptake and investigates the relative contribution of conidial uptake by AMs and AECs. Ultimately, our study highlights the importance of AMs for innate immunity but also reveals the relatively unexplored role of type 1 AECs as the host cell with the greatest potential leverage for fungal clearance in the early hours.

Results

We studied the relative contributions of alveolar epithelial cells (AECs) and alveolar macrophages (AMs) to the early immune response against *A. fumigatus* pursuing the bottom-up approach shown in Fig. 1. First, to link fungal uptake with conidial swelling in time, we fitted a Verhulst ODE model to the dynamically increasing conidial diameter based on re-analyzed experimental data from in vitro infection assays of type 2 AECs with *A. fumigatus* conidia^{35,36}. This enabled us to formulate a Malthus ODE model for the time-dependent uptake rate that is increasing as a result of the increasing contact area between the conidium and the host cell. We fitted this time-dependent uptake rate of type 2 AECs to the above-mentioned infection assays^{35,36} (see Fig. 1A–C). Next, we extended this mechanism to uptake by type 1 AECs and AMs and implemented these new features into our previously developed hybrid agent-based model (hABM)^{13,30,58–60} for the human alveolus. To explore the relative contributions of AECs and AMs to the uptake of *A. fumigatus* conidia, we ran millions of virtual infection scenarios with the hABM for the fitted uptake rate of type 2 AECs and screened over uptake rates for type 1 AECs and AMs (see Fig. 1D–F). In addition, we tested chemokine secretion onsets that are delayed by their dependence of conidial swelling with time, which affects the migration behavior of AMs, as well as the dynamic change in AM numbers within the alveolus. The mathematical details are explained in Methods in Extended hybrid agent-based model of the human alveolus, while Supplementary Video S1 illustrates the composition of the hABM and Supplementary Video S2 shows exemplary simulations of the hABM for the uptake by AMs, type 1 AECs, and type 2 AECs. Lastly, we trained a surrogate infection model (SIM), established in our previous study¹³, to interpolate the hABM simulation outcomes across the vast parameter space. The SIM enabled us to predict the relative uptake contributions of type 1 and type 2 AECs as well as AMs, allowing us to identify favorable parameter regimes for efficient clearance of *A. fumigatus* conidia from the human alveolus (see Fig. 1G). Based on our findings, we suggest new experimental efforts on type 1 AECs, as in almost all cases they are first exposed to *A. fumigatus* conidia and thus have the greatest impact in vivo.

Dynamics of conidial swelling is captured by the Verhulst ODE model

Conidia of *A. fumigatus* undergo swelling before the onset of hyphal growth that occurs around six hours post-infection. To study this early phase of infection, we exploited our experimental data obtained from infection assays of type 2 AECs and *A. fumigatus*^{35,36}. We re-analyzed the image data (see Methods in Experimental Data) and extracted the conidial diameter over time. Figure 2A shows that the Verhulst ODE model (dashed dark blue line) can be accurately fitted to the time-dependent conidial diameter (light blue points) reaching the lowest mean squared error (MSE) with $MSE = 0.5979$ compared to further baseline models (see Methods in Modeling the swelling of *A. fumigatus* conidia by a Verhulst ODE model, Supplementary Results 1.1 and Supplementary Figs. S1A, B, and fitted parameters in Supplementary Table S1). The model's sensitivity was investigated in Supplementary Results 1.2 where also the bootstrap method is described which was used to create the 95% confidence bands in Fig. 2. At the time $t = 0$ min, the conidial diameter is on average about $2.8\ \mu\text{m}$, swells over time reaching the

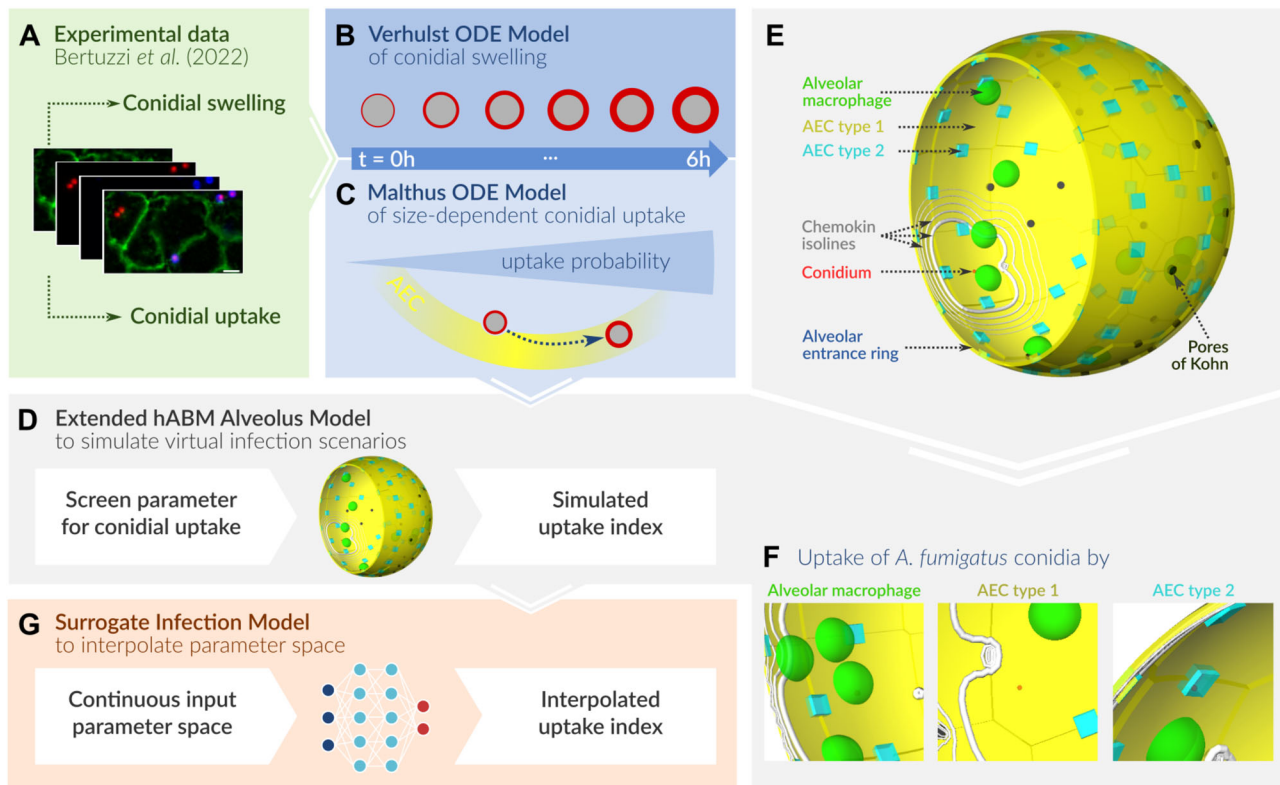


Fig. 1 | Bottom-up approach to model the immune response against *A. fumigatus* lung infection. **A–C** Based on experimental phagocytosis assays between *A. fumigatus* conidia and type 2 AECs (**A**), we fitted a Verhulst ODE model to the increase of conidial diameter (**B**), and an extended Malthus ODE model to uptake indexes resulting in an increasing chance of uptake from non-swelling to swelling conidia. The dotted arrow denotes the transition from a resting to a swelling conidium that is taken up with a higher probability (**C**). **D–F** Including the fitted ODEs into a previously developed hybrid agent-based model (hABM) of one human alveolus, we were able to simulate millions of virtual infection scenarios. The hABM comprises

one alveolus as a $\frac{3}{4}$ sphere consisting of type 1 AECs (yellow) and type 2 AECs (light blue). The entrance ring (dark blue) and pores of Kohn (PoK) (black) are the boundaries of the system (see Supplementary Video S1). The migration of AMs (green) is directed by the chemokine signal (white isolines) to locate the *A. fumigatus* conidia (red). The conidium can be taken up by AMs, type 1 and type 2 AECs, as demonstrated in the Supplementary Video S2. **G** By training a surrogate infection model (SIM) on the hABM output, we were able to predict uptake indexes by AMs and AECs for an interpolated parameter space.

exponential growth phase between times $t = 60$ min to $t = 120$ min and saturating with a diameter of about $4.6\mu\text{m}$ between times $t = 240$ min to $t = 300$ min.

Fitting the parameters of the Verhulst ODE model enabled us to retrieve the relative increase in the conidial area, which is shown by the dashed dark blue line in Fig. 2B. Starting from an area of 100% (denoted as a dark red point) in the resting state at time $t = 0$ min, we predict that the area increases to 103% at time $t = 60$ min, and further to 127%, 213% and 274% (denoted as red rings surrounding the red point) at times $t = 120$ min, $t = 180$ min and $t = 300$ min, respectively. We denoted this percentual surface area increase as a function of time, $S(t)$, with $S(t = 0\text{ h}) = 1.0$ and $S(t \geq 5\text{ h}) = 2.74$, e.g., 274% (see Fig. 2B and Methods in Modeling the swelling of *A. fumigatus* conidia by a Verhulst ODE model). As shown in Supplementary Fig. S1, the Verhulst ODE model can fit the temporal conidial diameter increase also for different experimental in vitro settings (see Methods in Experimental Data, Supplementary Results 1.1 and Supplementary Table S1), which underlines its general applicability to conidial diameter increase.

Malthus ODE model proposes conidial uptake to depend on time-dependent swelling

Exploring the mechanism of conidial uptake by type 2 AECs, we re-considered the experimental data from the infection assays^{35,36} that are displayed as the uptake index (red points) as a function of time in Fig. 2C. The uptake index corresponds to the percentage of conidia that are taken up based on the encountered conidia as a function of time post-infection and

yielded mean values of 15.5% at $t = 120$ min, 40.5% at $t = 240$ min and 62.2% at $t = 360$ min. To model the uptake dynamics, we derived and fitted a Malthus ODE model based on the assumption of a constant uptake rate r_{c-up} between conidium and type 2 AEC (see Methods in Modeling the uptake of conidia via an extended Malthus ODE model and Supplementary Results 1.3). However, as can be seen in Fig. 2C (orange dotted line), the fitted Malthus ODE does not reflect the dynamics of the mean values accurately for all experimentally measured time points. Next, we linked the Verhulst ODE model, which was fitted in the previous section for the dynamics of the conidial diameter and subsequent increasing surface area $S(t)$, to the uptake rate by type 2 AECs. The resulting extended Malthus ODE model is based on a time-dependent uptake rate governed by the conidial diameter (see Methods in Modeling the uptake of conidia via an extended Malthus ODE model). To test the overfitting and robustness of this derived extended Malthus ODE, cross-validation and sensitivity analysis was performed before the model was fitted to all data points exhibiting a lower $MSE = 0.098$ compared to $MSE = 0.101$ of the normal Malthus ODE (see Supplementary Results 1.2 and Supplementary Table S2). The optimal parameter was found to be $r_{up}^{AEC2} := r_{up}^{AEC2}(t = 0) = 0.00137\text{ min}^{-1}$ resulting in a time-dependent uptake parameter, $r_{up}^{AEC2}(t) = r_{up}^{AEC2} \cdot S(t)$ as shown by the dark red dashed curve in Fig. 2C. The confidence interval of the parameter r_{up}^{AEC2} was investigated in Supplementary Results 1.2. As can be seen in Fig. 2B, the time-dependent uptake rate $r_{up}^{AEC2}(t)$ reaches its maximum of approximately 274% of its initial value after 5 h, meaning $r_{up}^{AEC2}(t = 5\text{ h}) = 0.00137\text{ min}^{-1} \cdot 2.74 = 0.00375\text{ min}^{-1}$, that is when the contact area increases saturates.

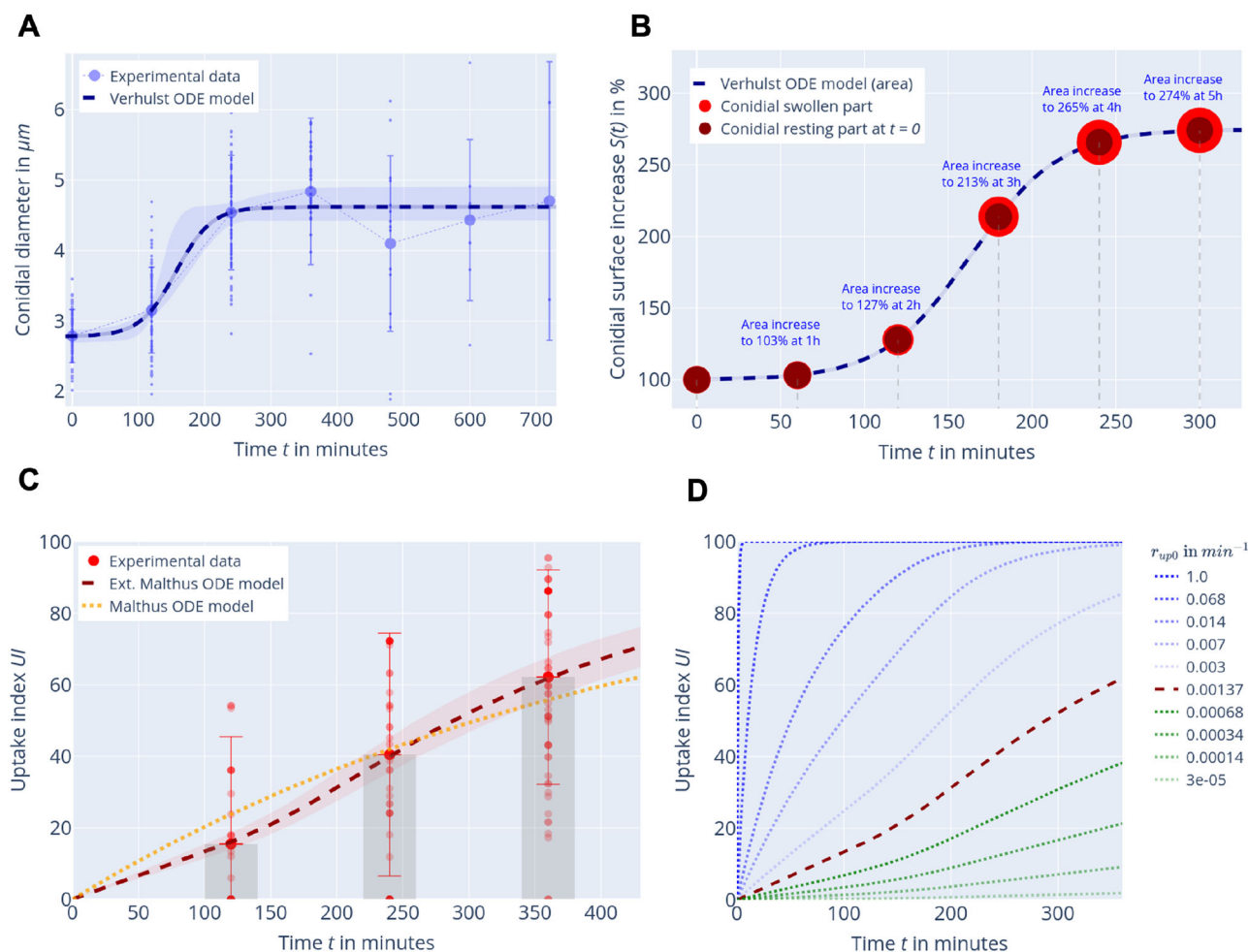


Fig. 2 | Modeling the conidial swelling and size-dependent uptake by type 2 AECs.

A The Verhulst ODE model (blue dashed line) exhibits the experimental conidial diameter in μm (blue points, mean values as big blue points) in the first 12 h. The blue shaded area represents the 95% confidence bands of the model prediction. **B** The Verhulst ODE model as the relative increase in area compared to $t = 0$ min (blue dashed line). The dark red dots represent the conidial size at $t = 0$ min and the red dots represent the swollen conidial part over time. **C** The extended Malthus ODE model (dark red dashed line) fitting the experimental size-dependent conidial

uptake by type 2 AECs (red points, mean values as big red points). The orange dashed line represents the normal Malthus ODE model. The red shaded area represents the 95% confidence bands of the model prediction. **D** The extended Malthus ODE model to model the theoretical uptake index for different uptake rates r_{up0} . Different opacity values for different values of r_{up0} for more (blue dotted lines) or less (green dotted lines) efficient uptake than type 2 AECs.

The fitted extended Malthus ODE links the increasing contact area between the conidium and the type 2 AEC to an increasing uptake rate of the type 2 AECs. This correlation has also been indicated previously for other host cells^{37,61,62}. Therefore, we use the extended Malthus ODE to model the uptake index of AMs (UI_{AM}), and type 1 AECs (UI_{AEC1}) with their respective uptake rates $r_{up0}^{AM}(t)$ and $r_{up0}^{AEC1}(t)$. Note that all uptake indexes UI_{HC} (or UI by HC) refer to the relative uptake indexes of a host cell (HC), calculated over the number of conidia that can be reached by the respective HC (see Methods in Input parameter and output measures for the extended hABM). The computed uptake indexes with the extended Malthus ODE can be seen in Fig. 2D for varying uptake rates. As elaborated in Supplementary Results 1.4, these are very accurate for stationary AECs that have permanent contact with the conidium but represent an upper limit for AMs that, prior to uptake, must migrate toward the conidium.

Uptake by type 1 AECs dominates the total uptake in the absence of AMs

In order to investigate the relative contributions of AECs and AMs to *A. fumigatus* uptake, we extended the hABM (see Methods in Extended hybrid agent-based model of the human alveolus) by implementing mechanisms simulating conidial swelling (Verhulst ODE model; see Methods in

Modeling the swelling of *A. fumigatus* conidia by a Verhulst ODE model) and size-dependent conidial uptake by type 1 and type 2 AECs as well as AMs (Malthus ODE model; Methods in Modeling the uptake of conidia via an extended Malthus ODE model). At first, we considered a scenario where only type 1 and type 2 AECs are present, i.e. we simulated the immune response in the human alveolus in the absence of AMs resembling a compromised immune status¹⁷. We used the fitted uptake rate $r_{up0}^{AEC2} = 0.00137 \text{ min}^{-1}$ for type 2 AECs and varied the uptake rate r_{up0} for type 1 AECs (see Table 1) based on a conducted literature search (see Supplementary Results 1.5 and Supplementary Table S3).

As shown by the light blue curve in Fig. 3A, the relative uptake by type 2 AECs (based on the total number of conidia confronted with type 2 AECs) reaches about 62% at time $t = 360$ min regardless of type 1 AEC uptake rates $r_{up0}^{AEC1}(t)$, as stationary type 1 and type 2 AECs do not compete over the conidium. Also, the extended Malthus ODE model (dashed dark red curve) is completely in line with the stochastic simulations for type 2 AEC uptake (light blue curve) as AECs are stationary and in direct contact with the conidium revealing the consistency of our simulation results with the analytical calculation. As shown in Fig. 3A, for time-dependent uptake rates of type 1 AECs $r_{up0}^{AEC1}(t) = r_{up0}^{AEC1} \cdot S(t)$, for $r_{up0}^{AEC1} \in \{0.000137, 0.000685, 0.00274\}$ in

Table 1 | The parameter ranges for the virtual experiments with the hABM

Parameter	Values
$r_{up0}^{AEC1} [min^{-1}]$	0.00137 · {0.1, 0.25, 0.5, 1.0, 2.0, 5.0}
$r_{up0}^{AM} [min^{-1}]$	0.00137 · {1, 10, 50, 200, 730}
$t_{sAEC} [min]$	0, 60, 120, 180, 240
n_{AM}	2, 4, 8, 12, 28

The parameters r_{up0}^{AEC1} and r_{up0}^{AM} determine the time-dependent uptake rates of type 1 AECs, and AMs. The parameter t_{sAEC} in minutes determines the time of onset of chemokine secretion and ranges from immediate ($t = 0$ min) to late ($t_{sAEC} = 240$ min) secretion. The parameter n_{AM} represents the number of AMs and ranges from a system with low numbers ($n_{AM} = 2$) to a system with increased AM numbers ($n_{AM} = 28$). For all combinations of parameter configurations, simulations were performed for the fitted uptake rate of type 2 AECs $r_{up0}^{AEC2} = 0.00137 min^{-1}$ and additionally for (i) no uptake by AECs with $r_{up0}^{AEC2} = r_{up0}^{AEC1} = 0.0$ and all AM numbers and ii) for no AM numbers, $n_{AM} = 0$ and all presented AEC uptake rates. For each described parameter combination, 10,000 infection scenarios of 480 min were simulated.

min^{-1} , corresponding to $0.1 \cdot r_{up}^{AEC2}(t)$, $0.5 \cdot r_{up}^{AEC2}(t)$ and $2 \cdot r_{up}^{AEC2}(t)$, (shown in dotted, dashed, and solid lines), respectively, we find that the overall uptake indexes of 11%, 38%, or 84% (orange lines) at six hours post-infection are entirely dominated by the relative uptake of the type 1 AECs (green lines). The reason for this somewhat non-intuitive result becomes clear from Fig. 3B, where we show that the total alveolar surface is mostly covered by type 1 AECs, such that the conidium will most likely (95.76%) be confronted with type 1 AECs rather than type 2 AECs. Thus, the uptake capacity of AECs mainly depends on type 1 AECs, simply because type 2 AECs will be rarely confronted with conidia (< 5%). In the absence of AMs, there is no cell movement and spatial impact which is why the results shown in Fig. 3A from the stochastic simulations confirm the analytical calculation (see Fig. 2D). Under conditions resembling a compromised immune status, we conclude that in the context of our stochastic model simulations (i), the uptake is entirely dominated by type 1 AECs and (ii) the uptake by AECs alone will not be sufficient to keep the alveolus free from conidia before fungal germination starts.

Uptake by AMs exceeds the total uptake by AECs

Next, simulating virtual infection scenarios that resemble the immunocompetent status, we included AMs to compare their relative contribution to fungal clearance in the human alveolus. Using the extended hABM, stochastic simulations were performed for varied uptake rates for type 1 AECs, r_{up0}^{AEC1} , and AMs, r_{up0}^{AM} , and the fitted uptake rate for type 2 AECs, $r_{up0}^{AEC2} = 0.00137 min^{-1}$. In addition, we screened over values for delayed onset of chemokine secretion t_{sAEC} by AECs as well as varied AM numbers n_{AM} . A detailed description of the screened parameters and their ranges, especially about shifted ranges for uptake by AECs versus uptake by AMs, is provided in the Methods in Input parameter and output measures for the extended hABM, Table 1 and the conducted literature search in Supplementary Results 1.5 and Supplementary Tables S3, S4. The hABM simulation results for an immunocompetent status are displayed in Fig. 3C–F, where we focused on the uptake indexes at six hours before fungal germination.

As can be seen in Fig. 3C, with an uptake of 88% and 70% (blue solid and dashed lines), AMs dominate the total uptake of conidia for type 1 AEC uptake rates $r_{up}^{AEC1}(t)$ with $r_{up0}^{AEC1} = 0.000685 min^{-1}$ (orange solid and dashed lines). In these scenarios for AM uptake rates $r_{up}^{AM}(t)$ with $r_{up0}^{AM} = 0.068 min^{-1}$ and $r_{up0}^{AM} = 0.014 min^{-1}$, AECs reach uptake indexes of about 12% (green solid line) and 23% (green dashed line), respectively. In both cases (dashed and solid lines), the impact of AMs increases rapidly with time as soon as chemokines are secreted starting from time $t_{sAEC} = 60$ min. The impact of the secretion onset t_{sAEC} can be seen in Fig. 3D in more detail; the later the onset of chemokine secretion is the longer AMs move randomly,

with a clear reduction in the relative uptake by AMs (blue solid and dashed lines) at six hours post-infection. In this case for $r_{up0}^{AM} = 0.274 min^{-1}$, $r_{up0}^{AEC1} = 0.00274 min^{-1}$, implying that the uptake rate of AMs is 100 times higher than that of type 1 AECs, the relative contribution of AECs rises from 38% to 49% when the secretion of chemokines starts relatively late at $t_{sAEC} = 180$ min instead of $t_{sAEC} = 120$ min, such that the relative uptake by AMs drops from 62% to 51%. As shown in Fig. 3E, a low AM uptake rate $r_{up}^{AM}(t)$ with $r_{up0}^{AM} = 0.00137 min^{-1}$ cannot be compensated by immediate chemokine secretion or high AM numbers (blue solid line) while the overall uptake does not reach more than 80% (orange solid line). In Fig. 3F, we consider the rather unrealistic scenario of an extremely high uptake rate of type 1 AECs with $r_{up0}^{AEC1} = 5 \cdot r_{up0}^{AEC2} = 0.068 min^{-1}$, being five times higher than the fitted uptake rate of type 2 AECs, which would make AECs the main player in uptake with a 75% contribution. In summary, the simulation results indicate that AMs clear the majority of *A. fumigatus* in most parameter regimes while AECs can compensate to a certain extent but remain important for guidance through chemokine signaling.

Surrogate model reflects fungal infection dynamics and assesses model sensitivity

To fully exploit the hABM simulation data, we previously established a surrogate infection model (SIM) based on a Multilayer Perceptron (MLP)¹³ and fitted it to the simulation data by the hABM as described in Methods in the surrogate infection model using a multilayer perceptron. The SIM-enabled us to interpolate between all simulated values of the large input parameter space accurately and predicted uptake indexes of AECs (UI_{AEC}) and AMs (UI_{AM}), described in Methods in input parameter and output measures for the extended hABM, for a specific time point that are otherwise computed by time-intensive hABM simulations.

We applied the SIM to perform a global sensitivity analysis of the hABM using the Sobol sensitivity analysis⁶³ to assess the influence of the input parameter (r_{up0}^{AEC1} , r_{up0}^{AM} , t_{sAEC} , n_{AM}) on the uptake indexes UI_{AEC} and UI_{AM} at the timepoint $t = 6h$. As shown in Fig. 4A, the uptake rate r_{up0}^{AEC1} of type 1 AECs has the largest impact in first-order (green bar) with a Sobol index of 0.7 and total-order (green striped bar) with a Sobol index of 0.75 on the uptake index of AECs UI_{AEC} . The remaining parameters have low impacts with Sobol indexes below 0.2. In comparison, the uptake index of AMs UI_{AM} is most influenced by their uptake rate r_{up0}^{AM} (see Fig. 4B), even though not as dominant with a Sobol index of 0.42 (first-order, blue bar) and 0.48 (total-order, blue striped bar). For the uptake by AMs, UI_{AM} , also the uptake rate r_{up0}^{AEC1} and the number of AMs n_{AM} play a non-negligible role with Sobol indexes between 0.2 and 0.3. The impact on both uptake indexes by the delay of chemokine secretion t_{sAEC} is the lowest with Sobol indexes below 0.1. In all cases, the total-order measures are higher than the first-order measures indicating a highly non-linear and complex system. Our analysis underlines the importance of the uptake rates of AECs and AMs.

AMs are indispensable for the clearance of *A. fumigatus* in the human alveolus

Using the outputs UI_{AEC} , UI_{AM} of the SIM, we evaluated several measures to gain insights about the infection dynamics in the hABM: i) the difference between UI_{AEC} and UI_{AM} to assess which cell type contributes more to conidial uptake (uptake comparison (UC)), (ii) the total uptake index (UI), which we defined as the sum of UI_{AEC} and UI_{AM} (see Methods in Input parameter and output measures for the extended hABM) and (iii) relative uptake contributions for AECs, $UI_{AEC}/(UI_{AEC} + UI_{AM})$, and for AMs, $UI_{AM}/(UI_{AEC} + UI_{AM})$ (see Methods in Input parameter and output measures for the extended hABM and The surrogate infection model using a multilayer perceptron).

In Fig. 5, we present the SIM predictions for an average AM number of $n_{AM} = 12$. With an immediate (left plots), as well as delayed onset of chemokine secretion ($t_{sAEC} = 90$ min) (middle plots), AMs clear the infection in the majority of scenarios reaching high values of $UI = 100\%$ (see Fig. 5A left and middle plot). Upon late chemokine secretion, starting at

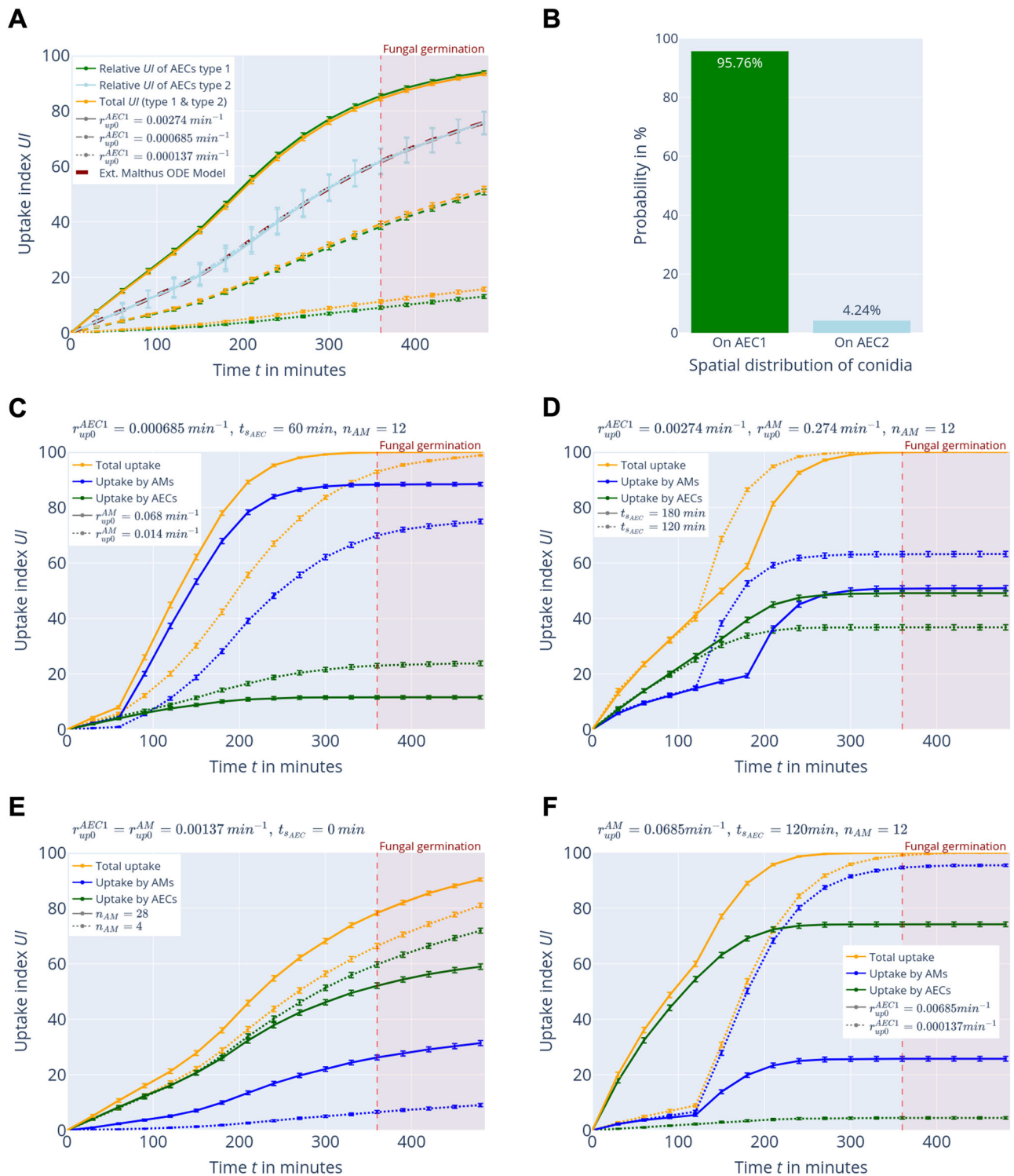


Fig. 3 | Simulation results of the extended hABM. A The hABM simulations results without AMs. The light blue line shows the relative uptake by type 2 AECs matching the analytical solution from the extended Malthus ODE Model (dark red dotted). The green curves show the relative uptake by type 1 AECs, and the orange lines show the overall uptake by AECs. Different line styles denote different values of r_{up0}^{AEC1} . **B** The spatial distribution of conidia being confronted with type 1 or type 2 AECs averaged over all hABM simulations. **C–F** The blue lines denote the uptake by AMs, and the green lines denote the uptake by type 1 and type 2 AECs combined. The

orange lines denote the overall uptake. The corresponding parameter combination is written at the top. In (**C**), different line styles denote different values of r_{up0}^{AM} . In (**D**) different line styles denote varied delayed chemokine secretion t_{sAEC} scenarios. In (**E**) different line styles denote different AM numbers n_{AM} . In (**F**) different line styles denote different values of r_{up0}^{AEC1} . In (**A**, **C–F**) error bars represent the 95% confidence interval as obtained from the standard error of independent Bernoulli trials.

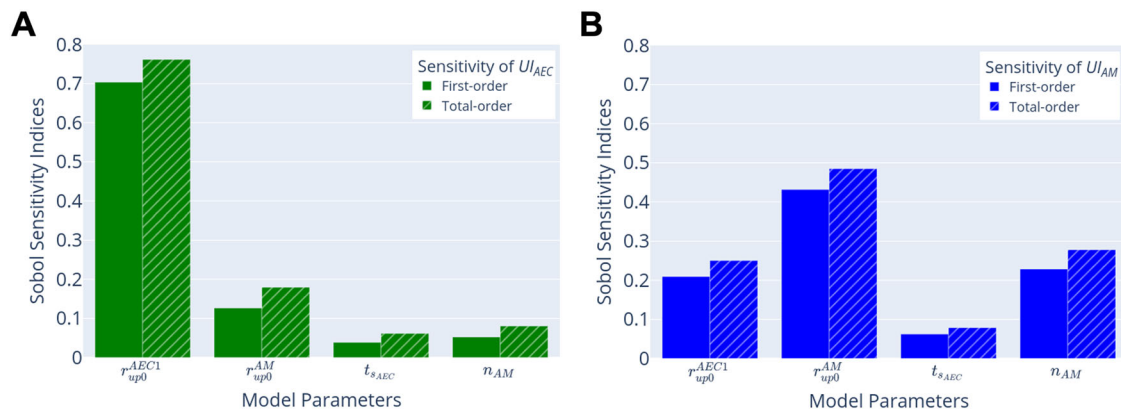


Fig. 4 | Sobol sensitivity analysis of the hABM with the SIM. A Relative impact of the input parameters on the uptake index of AECs UI_{AEC} in the hABM is denoted with the Sobol index. **B** Relative impact of the input parameters on the uptake index of AMs UI_{AM} in the hABM denoted with the Sobol index.

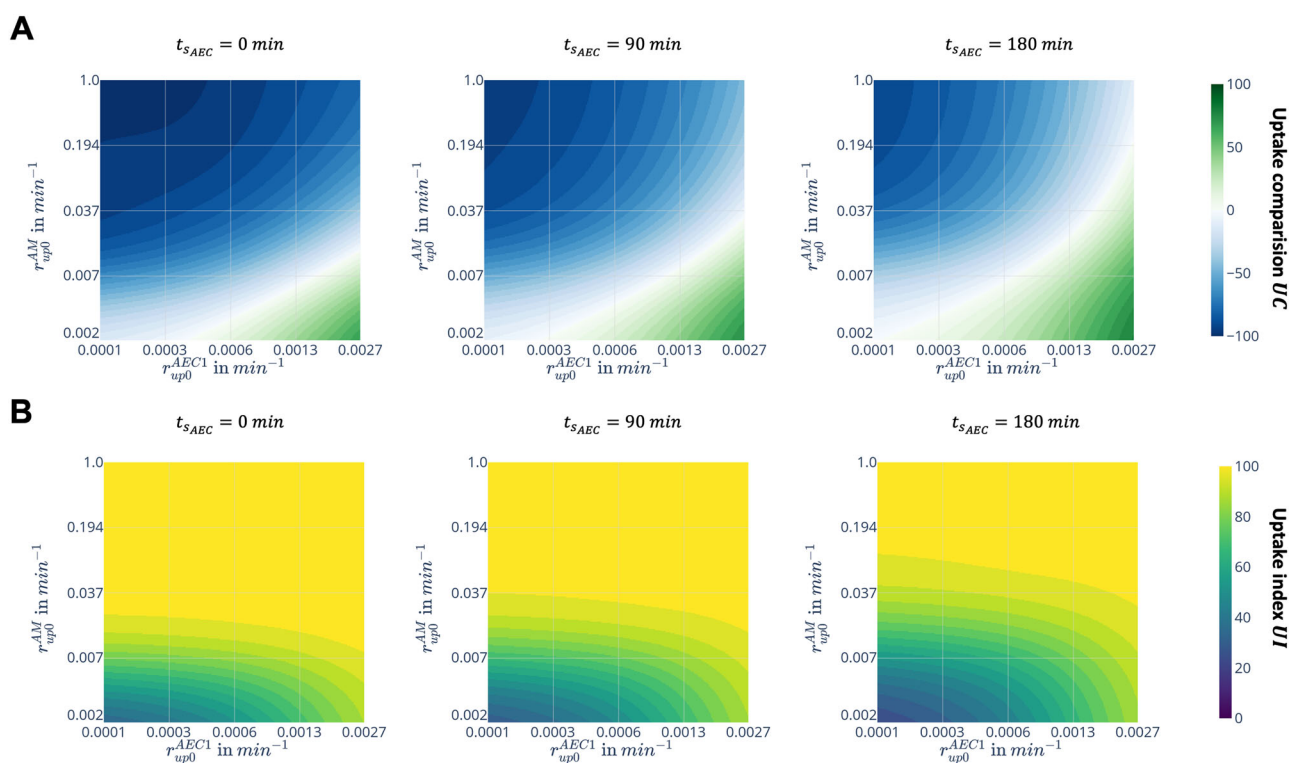


Fig. 5 | Predictions with the SIM for varying onsets of chemokine secretion.

A, B Uptake comparisons and indexes at the onset of germination at $t = 360 \text{ min}$. All plots denote on the x-axis the time-dependent uptake rate $r_{up0}^{AEC1}(t) = r_{up0}^{AEC1} \cdot S(t)$ for varying r_{up0}^{AEC1} for type 1 AECs and on the y-axis the time-dependent uptake rate $r_{up0}^{AM}(t) = r_{up0}^{AM} \cdot S(t)$ for varying r_{up0}^{AM} . The plots are displayed for low $t_{sAEC} = 0 \text{ min}$, medium $t_{sAEC} = 90 \text{ min}$ and high $t_{sAEC} = 180 \text{ min}$ onsets of chemokine secretion

for an average AM number of $n_{AM} = 12$. Predicted UI and UC values are rounded to integers dividable by five for better visibility of UI and UC structures. **A** The color-coded uptake comparison UC denotes in green (positive values) that AECs take up more conidia and in blue (negative values) that AMs take up more conidia. **B** The color-coded uptake index UI denoting in blue a low and in yellow a high overall uptake index of 100% by AMs and AECs combined.

$t_{sAEC} = 180 \text{ min}$ (right plot in Fig. 5A), the AECs' relative contribution increases, denoted by the increased green area, but concurrently worsen overall uptake of $UI < 95\%$ for $r_{up0}^{AM} < 0.037 \text{ min}^{-1}$ (right plot Fig. 5B). In Fig. 6, SIM predictions are shown for AM numbers ranging from low ($n_{AM} = 4$, left plots) and average ($n_{AM} = 12$, middle plots) to high ($n_{AM} = 28$, right plots) and for the onset of chemokine secretion at $t_{sAEC} = 60 \text{ min}$. For reduced AM numbers $n_{AM} = 4$, AECs can support, but only high uptake rates $r_{up0}^{AM}(t)$, $r_{up0}^{AEC1}(t)$ with $r_{up0}^{AM} > 0.19 \text{ min}^{-1}$ and $r_{up0}^{AEC1} > 0.0013 \text{ min}^{-1}$ (right upper corner in Fig. 6A and Fig. 6B left plots) were found to be sufficient to reach high values $UI = 100\%$. For high AM

numbers of $n_{AM} = 28$, AM uptake rates $r_{up0}^{AM}(t)$ with $r_{up0}^{AM} > 0.01 \text{ min}^{-1}$ were sufficient for AMs to surpass the uptake contribution by AECs (blue area in Fig. 6B right plot) and simultaneously reach a high overall clearance of $UI = 100\%$ (yellow area in Fig. 6A right plot). For all scenarios in Figs. 5, 6, we found that, for low uptake rates with $r_{up0}^{AM} < 0.0068 \text{ min}^{-1} \approx 5 \cdot r_{up0}^{AEC2}$ for AMs, even high uptake rates with $r_{up0}^{AEC1} = 0.0027 \text{ min}^{-1} \approx 2 \cdot r_{up0}^{AEC2}$ for type 1 AECs, being twice as high as the uptake rate by type 2 AECs, was not sufficient to reach $UI = 100\%$ the screened regime of parameters. Ultimately, in Fig. 7, we consider the uptake rates of AMs $r_{up0}^{AM} \in [0.037, 0.19] \text{ min}^{-1}$ (the second rows in each plot in Figs. 4 and 5) and compare the

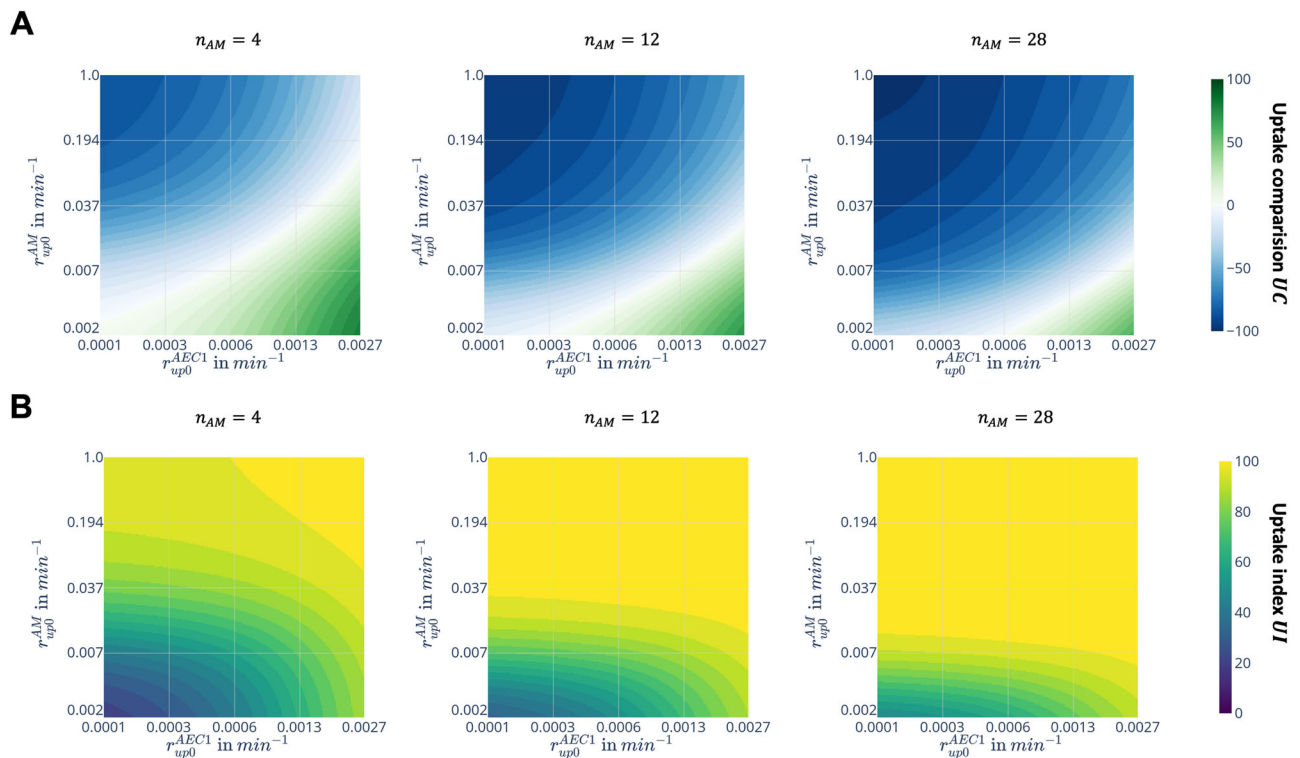


Fig. 6 | Predictions with the SIM for varying AM numbers. A, B Uptake comparisons and indexes at the onset of germination at $t = 360$ min. All plots denote on the x-axis the time-dependent uptake rate $r_{up}^{AEC1}(t) = r_{up}^{AEC1} \cdot S(t)$ for varying r_{up}^{AEC1} type 1 AECs and on the y-axis the time-dependent uptake rate $r_{up}^{AM}(t) = r_{up}^{AM}(t=0) \cdot S(t)$ for varying r_{up}^{AM} . The plots are displayed for low ($n_{AM} = 4$), average ($n_{AM} = 12$), and high ($n_{AM} = 28$) AM numbers and onsets of chemokine secretion

at $t_{s_{AEC}} = 60$ min. Predicted UI and UC values are rounded to integers dividable by five for better visibility of UI and UC structures. **A** The color-coded uptake comparison UC denotes in green (positive values) that AECs take up more conidia and in blue (negative values) that AMs take up more conidia. **B** The color-coded uptake index UI denoting in blue a low and in yellow a high overall uptake index of 100% by AMs and AECs combined.

relative uptake contributions of AECs (green curves) and AMs (blue curves). We can see that for an immediate chemokine secretion, AECs do not reach more than 20% contribution (Fig. 7A left), while this goes up to more than 30% if chemokine secretion starts late $t_{s_{AEC}} = 120$ min (Fig. 7A right), in case we assume $r_{up}^{AEC1} = r_{up}^{AEC2}$. For low and high AM numbers in the exemplary combinations in Fig. 7B, the contribution of AECs does not become more than 40%. This underlines the importance of uptake by AMs as the professional resident phagocytes, and that this cannot be compensated by early onsets of chemokine secretion, high AM numbers, or increased uptake rates by type 1 AECs.

Discussion

In this study, we investigated the relative contributions of alveolar epithelial cells (AECs) and alveolar macrophages (AMs) in the internalization of swelling *A. fumigatus* conidia during the first hours post-infection. Based on recently performed in vitro experiments^{35,36} on the uptake of conidia by type 2 AECs, we were able to fit a Verhulst ODE model to conidial diameter data and coupled the dynamics of swelling with an extended Malthus ODE model. We fitted the system of ODEs to the size-dependent uptake of conidia by type 2 AECs hypothesizing that swelling increases the observed uptake probability during the first six hours (see Fig. 1A–C and Fig. 2). We extended this mechanism to uptake by type 1 AECs and AMs and studied the dynamics with computer simulations using a previously developed hybrid agent-based model (hABM)^{13,30,58–60} for the human alveolus (see Fig. 1D–F and Fig. 3). Using the hABM, we ran millions of stochastic virtual experiments to simulate the first hours of immune response in the human lung against *A. fumigatus* conidia and screened over various uptake rates of type 1 AECs and AMs, delayed onsets of chemokine secretion, induced by a swelling conidium, as well as the impact of varying AM numbers. Using the

hABM simulations results, we trained a surrogate infection model (SIM) to interpolate the parameter space, assessed the sensitivity of the hABM (see Fig. 4), and predicted the uptake proportions of AECs compared to AMs and the overall clearance of *A. fumigatus* conidia (see Fig. 1G and Figs. 5, 6 and 7).

We fitted a Verhulst ODE model to the diameter of swelling conidia over time exhibiting a logistic growth curve saturating at around a diameter of $4.6\mu\text{m}$ or area increase 274% in comparison to $t = 0$ min. As these dynamics can depend on the strain of *A. fumigatus* (here: A1160⁺), the growth medium or the underlying cells (here: immortalized A549 cells, used as a model for human type 2 AECs), we also fitted the Verhulst ODE model to two other experimental settings resulting in comparable parameter settings (see Supplementary Table S1) which shows a general logistic increase of conidial surface area during the first hours post-infection. In all cases, we found the exponential growth phase to start approximately at around one hour, until it slows down after three hours and saturates after approximately four to five hours. The lung provides a warm and humid environment offering ideal growth conditions. These are mimicked in the utilized in vitro data retrieved from experiments on type 2 AECs, which lets us expect a comparable development of *A. fumigatus* in the lung. Based on the conidial diameter increase, we fitted a second model – an extended Malthus ODE model – to simulate the uptake of conidia by type 2 AECs, as constant uptake rates do not reflect temporal uptake indexes, which is why we coupled the mechanism with the swelling-induced increased contact area between conidia and host cell. This is because once the conidium starts to swell as part of the germination process, the melanin layer in the cell wall undergoes structural changes leading to an increased number of exposed pathogen-associated molecular patterns (PAMPs). Consequently, the increased contact area between conidia and host cell makes conidia more accessible for pattern recognition receptors (PRRs) such as Toll-like receptors (TLRs) and

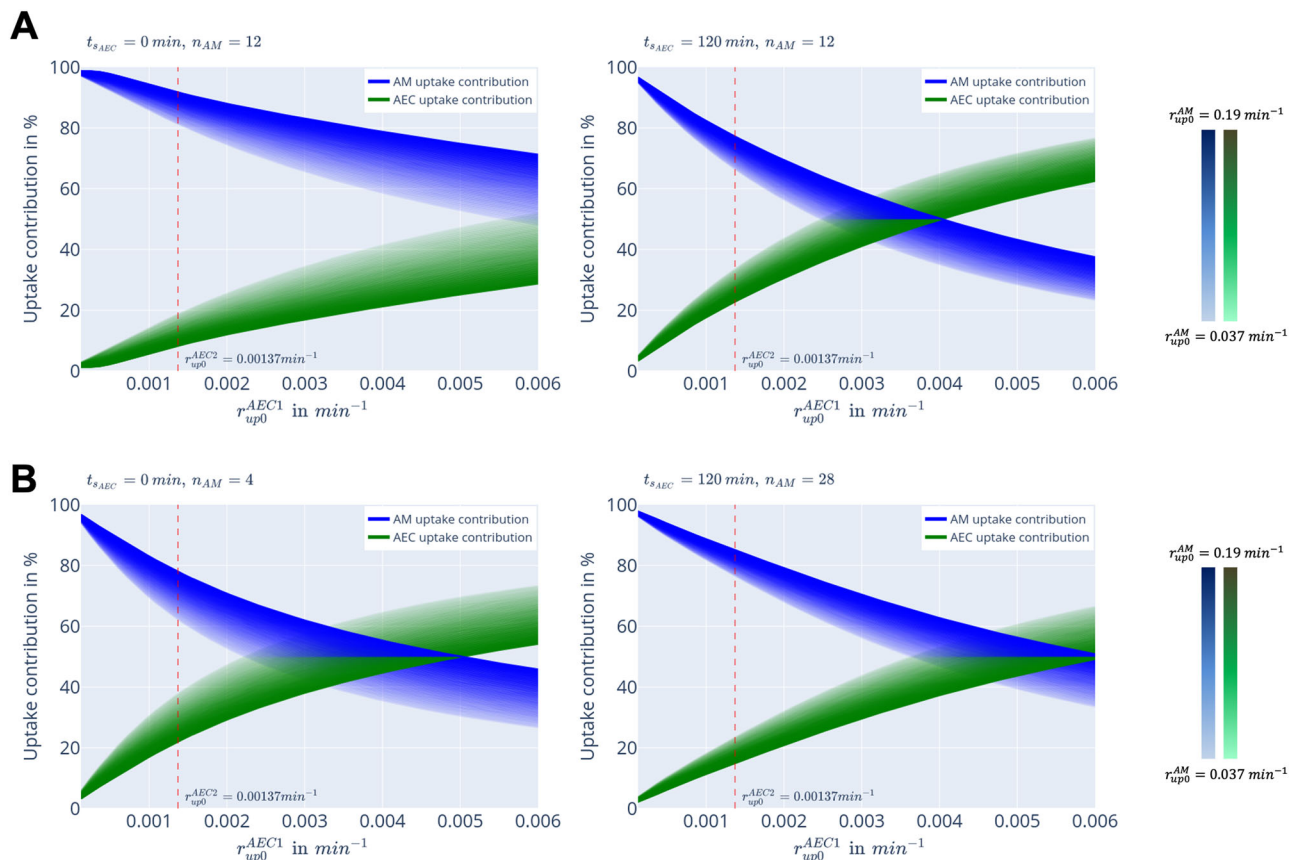


Fig. 7 | Predictions with the SIM for the clearance contributions of the hABM.

A, B Uptake contribution of AMs compared to AECs (y-axis) given on the x-axis the time-dependent uptake rate $r_{up}^{AEC1}(t) = r_{up0}^{AEC1} \cdot S(t)$ for varying r_{up0}^{AEC1} for type 1 AECs. Different opacities of the blue and green curves stand for high (dark) down to low (bright) values of the time-dependent uptake rate $r_{up}^{AM}(t) = r_{up0}^{AM} \cdot S(t)$ for varying r_{up0}^{AM} AMs. The blue curves denote the relative uptake contribution by AMs, and the green curves denote the relative uptake contribution by type 1 and type 2

AECs combined. The values are normalized, such the sum of two curves for the same value of r_{up0}^{AM} adds up to 100. **A** Predictions for $n_{AM} = 12$, $t_{sAEC} = 0$ min (left) and $t_{sAEC} = 120$ min (right). **B** Predictions for low AM numbers and early onset of chemokine secretion $n_{AM} = 4$, $t_{sAEC} = 0$ min (left) and for high AM numbers and late onset of chemokine secretion $n_{AM} = 28$, $t_{sAEC} = 120$ min.

C-type lectin receptors (CLRs). The binding of PAMPs to PRRs triggers immune reactions and makes the conidia susceptible to being recognized and internalized by host cells. Therefore, the increased diameter can be seen as an implicit measure for the number of PAMP-PRR bindings on the conidial surface. The fact that swollen conidia are taken up faster by AMs and AECs than resting conidia is well-known^{37,62} and supports our modeling approach that incorporates the increasing contact area driving the increase of uptake rates as a function of time, a proposed mechanism that is yet to be tested experimentally. Moreover, it is speculated that AECs do not necessarily start to secrete chemokines at first contact, but that this is a delayed process during the first hours post-infection^{45,64,65}. We assume that the underlying AEC is required to recognize a substantial change in the number of visible PAMPs on a conidium becoming apparent with the increasing size of conidial swelling. Once a threshold of PAMP-PRR is reached, intracellular pathways of the AEC become sufficiently activated to induce the secretion of pro-inflammatory cytokines and chemokines. In our simulations, the various thresholds of the number of visible PAMPs that trigger the chemokine secretion are modeled by the delayed chemokine secretion onset t_{sAEC} . Since the size of the conidium does not increase remarkably anymore after four hours, we assume that the melanin layer is largely dissolved with the number of visible PAMPs saturating around this time. Thus, the cascade of innate immune response is activated before, which is evidenced by experiments where various cytokines could already be measured at four hours post-infection⁶⁶. Based on these experimental findings, we assumed the most probable period for the onset of chemokine secretion to be between one and two hours, and not later than three hours, corresponding to the time

window when the conidial diameter increase enters the exponential phase. Future studies should focus on extending the simulations beyond six hours post-infection, where germination of conidia will start. Simulating the germination process as a function of time will enable quantifying the conditions under which conidia will be able to cross the *valley of death*. This is the time span between the start of conidial swelling and the onset of germination, where the probability of conidial detection is increased due to the expression of PAMPs by the conidia and the chemotactic guidance of AMs. We expect that the *valley of death* will be crossed by those conidia that relatively quickly swell, germinate, and develop hyphae that cannot be phagocytosed by AMs but require the recruitment of neutrophils to the alveolus⁴⁶.

We included the described ODE models into a previously developed hABM^{13,30,58–60}. We used this model of one human alveolus with fitted (type 2 AECs) and screened uptake rates (type 1 AECs and AMs) to simulate virtual infection scenarios in the human lung (see Fig. 1D–F and Supplementary Videos S1, S2). However, at first, we simulated scenarios for a compromised system in the absence of AMs. It was recognized that even for a high type 1 AEC uptake rate $r_{up}^{AEC1}(t)$ with $r_{up0}^{AEC1} = 0.00274 \text{ min}^{-1}$, which is twice as high as for type 2 AECs, the overall uptake by type 1 and type 2 AECs combined, does not reach sufficient uptake indexes of more than 90% at six hours post-infection, so it would be unable to completely prevent fungal germination. Furthermore, the overall uptake is mainly dominated by type 1 AECs because they cover around 95% of the lung surface as also confirmed in the to-scale extended hABM. This means that, even though type 2 AECs outnumber type 1 AECs, they are barely confronted with microbial

invaders, which makes their direct role in fungal clearance minor. However, in vitro experiments are typically conducted with type 2 AECs due to established protocols and cultivation, which are then used to estimate uptake rates also for type 1 AECs. This can lead to a strong under- or overestimation of the general role of AECs, e.g., in case type 1 AECs take up significantly more or less than type 2 AECs. Because of this gap in the data, we suggest increasing experimental efforts for studies with type 1 AECs, as they can have a large positive or negative leverage for infection clearance.

We also used the hABM to run immunocompetent infection scenarios with the fitted uptake rate for type 2 AECs and varied the uptake rates of type 1 AECs and AMs. Moreover, we screened over a delayed onset of chemokine secretion by AECs and varying AM numbers, both impacting the uptake efficiency of AMs. The simulation results showed that AMs can unfold their full proficiencies through initiated chemotactic migration, the moment the AMs sense the chemokine gradient, which lets the uptake indexes increase steeply. AECs have a supportive role when the efficiency of AM uptake is reduced but can usually not compensate to reach high overall uptake indexes $UI = 100\%$. For an average AM number $n_{AM} = 12$, AMs dominate the majority of cleared infection scenarios. Thus, even though their accumulated surface area covers only about 3% of the alveolar surface, the impact of AMs is compensated by their ability to migrate in the alveolus. However, this necessary detection process by AMs leads to a deviation between the expected AM uptake indexes by the extended Malthus ODE and the uptake indexes retrieved by the hABM simulations. As a result, we assume that estimating AM uptake rates from experimental studies for the hABM in the same way as for AEC uptake rates leads to an underestimation, as uptake by AMs in the hABM is a process of conidial detection and uptake itself, in contrast to uptake by AECs whose detection time is zero (see Supplementary Results 1.4 and Supplementary Fig. S3). Interestingly, as we observed in the spatiotemporal hABM simulations, the conidium can be confronted with more than one AM at the same time, which multiplies their chance of uptake by AMs. On the contrary, only one AEC at a time can be in contact with the conidium, because the AECs are stationary cells forming the cellular wall of the alveoli. As we have shown previously, we expect AMs to be able to clear the infection for low infection doses in most cases, only for high infection doses or low AM activity neutrophils are recruited to the site of infection⁴⁶ to reduce the risk of unwanted host cell damage due to a high inflammation⁶⁷.

Lastly, we trained a SIM on the hABM simulation results to assess the sensitivity of the hABM and to interpolate the input parameter space allowing us to conduct a fast and accurate analysis of the uptake comparison and the uptake index. Since the healthy human lung is generally not at risk of *A. fumigatus* infections, we can narrow down the parameter space to regimes for which the predicted uptake indexes reach $UI = 100\%$. The conidial uptake is dominated by AMs in these parameter regimes, except for rare cases where the uptake rates of type 1 AECs exceed the fitted uptake rate of type 2 AECs by factors that are at least two-fold higher. However, the exact uptake rates of AMs are difficult to determine experimentally since it is not a simple measure of alive conidia at a certain time point but depends on experimental conditions such as the cell density or environment. In addition, these measurements are mostly global, while the uptake rates in our agent-based approach work locally per immune cell. This matter was further analyzed in Supplementary Results 1.4 and Supplementary Fig. S3 elaborating how uptake indexes measured in our hABM simulations are connected to actual local uptake rates per cell. Based on this analysis, we expect that experimentally measured uptake rates are a lower bound for time-dependent uptake rates of AMs. Together with the broad literature search that we conducted (see Supplementary Results 1.5 and Supplementary Table S3), we attempt to predict the parameter ranges for uptake rates: Wasylnka et al.⁶⁸ reported that 98% conidia were killed by AMs in mice at 6 hours post-infection, which leads to an estimated uptake rate of $r_{up0}^{AM} \gg 0.0056 \text{ min}^{-1}$. Apart from the neglected detection time, only the killed conidia were measured, but since the percentage of taken-up conidia is higher than the percentage of killed conidia, the true uptake rate is expected to be higher. From Philippe et al.⁶¹, we derive an uptake rate measured at

$t = 240 \text{ min}$ which translates to increased $r_{up0}^{AM} \gg 0.0061 \text{ min}^{-1}$ because of not measured AM migration time. Based on the exact experimental conditions, these actual uptake rates can be higher by at least one order of magnitude due to necessary AM migration and conidial detection time (see Supplementary Results 1.4 and Supplementary Fig. S3), which let us expect AM uptake rates approximately at least at $r_{up}^{AM}(t) > 0.05 \text{ min}^{-1}$. Regarding the uptake rates of stationary AECs, there is less uncertainty between experimentally derived uptake rates and model uptake rates since there is immediate contact between the conidium and the host cell. However, measurements of uptakes by AECs type 2 human cells of type A549 still vary. Keizer et al.⁶⁹ measured 75% to 81% taken up after 4 hours across different strains leading to an AEC type 2 uptake rate of up to $r_{up0}^{AEC2} = 0.0044 \text{ min}^{-1}$, which were the highest values we could find. It also indicates transferability between isolates⁷⁰. On the contrary, for one of these isolates (ATCC46645), Seidel et al.⁷¹ found only 30% of conidia taken up after 6 h reaching only $r_{up0}^{AEC2} = 0.0005 \text{ min}^{-1}$. In the same study, it was reported that AECs have difficulties to kill conidia efficiently and could rather be used by *A. fumigatus* as an immune evasion pathway, which would once more emphasize the necessity of effective AMs regarding uptake and killing. In total, as there is no data on type 1 AECs and based on experimental type 2 studies, we expect uptake rates of AECs type 1 and type 2 not to be higher than $r_{up}^{AEC1}(t) < 0.005 \text{ min}^{-1}$. Together with the hABM simulations for competent AMs (sufficient uptake, numbers, and signaling), an uptake contribution of AECs lower than 30% is indicated. However, in case of surprisingly high (or low) uptake rates of type 1 AECs, the uptake contribution can go steeply up (or down) because the contribution of AECs during fungal clearance by phagocytosis is dominated by type 1 AECs which is why determining the uptake rate by type 1 AECs is crucial. This is also indicated by our sensitivity analysis with the uptake rate of type 1 AECs exhibiting the highest Sobol indexes. Available studies on the uptake of nanoparticles by type 1 AECs were conducted⁷², but insights are difficult to transfer to much larger *A. fumigatus* conidia. In conclusion, studies in vivo and in vitro generally show that uptake rates of AMs are higher than uptake rates of AECs, as expected for professional phagocytes (see Supplementary Table S3), but based on available data, their actual values can only be narrowed down, since they depend on cell types, *A. fumigatus* strains, and general experimental conditions. To tackle the above-mentioned gap in the data about conidial response to type 1 AECs, but also validating predicted uptake rates of AMs and AECs for different conditions by our modeling approach, more experimental efforts are necessary in the form of combined phagocytosis assays measuring the proportion of taken up conidia over time. To study these cross-cellular systems, advanced in vitro methods for example organ-on-chips models^{73–75} are suitable as they also model complex cell-to-cell interactions in a realistic system, e.g., whether AECs take up less in the presence of AMs or when neutrophils migrate to the site of infection, mimicking the in vivo situation but keeping the variables under control.

In summary, our virtual infection modeling approach consisting of a system of ODEs fitted to experimental data and an established hABM of one human alveolus, proposes a size-dependent uptake mechanism of *A. fumigatus* conidia that remains to be experimentally tested. Using predictive modeling, we narrowed down the ranges for unknown uptake parameters as well as for the onset of chemokine secretion by AECs in the context of the hABM. Based on these in silico findings that need to be tested in vitro as a subsequent step, our simulations suggest that AMs are the dominant player in clearing the lung from *A. fumigatus* conidia, while AECs can contribute to a minor extent with potential leverage, largely depending on type 1 AEC uptake rates. However, an important role for AECs also lies in their function to early secrete chemokines and direct AMs more efficiently toward the conidia. Additionally, based on our spatiotemporal simulations, and a broad analysis of available literature, we also suggest increasing efforts in studying type 1 AECs. They cover around 95% of the pulmonary surface area and are constantly confronted with not only conidia but all types of microbial invaders. Uncovering the functionality of type 1 AECs and their differences from type 2 AECs will be crucial for filling the gaps in our understanding of early pulmonary innate immunity.

Methods

Experimental data

The experimental data at the base of this work was derived from newly generated germination data (Supplementary Fig. 1A) and in vitro infections presented in Bertuzzi et al.^{35,36} (Figs. 1B and 2B). There, germination of A1160⁺ conidia (Rizzetto et al., 2013) was evaluated in 24-well plate format with 1.05×10^5 conidia/cm² (4×10^5 conidia/mL) in supplemented DMEM (10% fetal bovine serum (FBS), 1% penicillin/streptomycin cocktail) at 37 °C, 5% CO₂ every hour for 16 h. Cell area (μm²) and shape (aspect ratio) were quantified using a custom ImageJ algorithm (Ortiz et al., (In preparation, see Supplementary Results 1.1) across three replicate wells and over 1000 cells per replicate. For in vitro infection experiments, 200 μl of a 10^6 spore/ml suspension of the *A. fumigatus* strain A1160^{+/tdIT} (genetically modified to constitutively express the red fluorescent protein tdTomato). The data of Bertuzzi et al.^{35,36} was initially used for infections of the human pulmonary carcinoma epithelial cell line A549 (American type culture collection, CCL-185) at a MOI 0.5 (with 10^5 AECs in a >90% confluent monolayers). The infected cells were incubated at 37 °C, 5% CO₂ for the indicated hours, when single-cell analyses of the uptake of tdTomato-expressing *Af* strains via differential fluorescent staining with the chitin-binding cell-impermeant dye Calcofluor White by cultured AECs were performed as described in Bertuzzi & Howell, 2021⁷⁶. After identification of *A. fumigatus*-AEC interaction events using the IDEAS® software, for each time-point of infection (30 min, 2, 4 and 6 h post-infection), fungal area (μm²) and shape (aspect ratio) of internalized and adherent *A. fumigatus* A1160^{+/tdIT} AECs ($n = 10$ –160 for each time-point, 2 biological replicates) were measured using Image J version 1.53c.

Modeling the swelling of *A. fumigatus* conidia by a Verhulst ODE model

To mechanistically model conidial swelling in terms of the conidial diameter *Diam* in μm, we assumed that the conidial diameter consists of a constant initial diameter (*Diam*_{rest}), representing the size of a resting conidium, and a part that increases due to conidial swelling (*Diam*_{swell}(*t*)). The time-dependent diameter of the conidium is given by *Diam*(*t*) = *Diam*_{rest}(*t*) + *Diam*_{swell}(*t*), where we modeled the swelling part *Diam*_{swell} using a Verhulst ODE model, which represents a logistic growth model:

$$\frac{d[Diam_{swell}]}{dt} = r_{swell} \cdot [Diam_{swell}] \left(1 - \frac{[Diam_{swell}]}{C_{swell}} \right), \quad (1)$$

$$Diam_{swell}(t = 0) = D_{swell}^0$$

with swelling rate r_{swell} , the carrying capacity C_{swell} in μm as well as the swelling diameter D_{swell}^0 in μm at time $t = 0$ min. The constant resting part is represented by one parameter $Diam_{rest}(t) = D_{rest}^0$ with $d[Diam_{rest}]/dt = 0$. Therefore, we have $d[Diam]/dt = d[Diam_{swell}]/dt$. The analytical solution of *Diam*(*t*) is given as:

$$Diam(t; \Theta_{diam}) = \frac{C_{swell}}{D_{swell}^0 + (C_{swell} - D_{swell}^0)e^{-r_{swell} \cdot t}} D_{swell}^0 + D_{rest}^0 \quad (2)$$

with the diameter at $t = 0$ referring to the size of the conidium when it enters the alveolus: $Diam(t = 0) = D_{swell}^0 + D_{rest}^0$. We fitted the model parameters $\Theta_{diam} = (r_{swell}, C_{swell}, D_{swell}^0, D_{rest}^0)$ by minimizing the mean squared error (MSE):

$$MSE_{diam}(\Theta_{diam}) = \frac{1}{N} \sum_{i=0 \dots N} (Diam(t_i; \Theta_{diam}) - Diam_{data}(i))^2 \quad (3)$$

The data points *Diam*_{data}(*i*) exhibits all $i = 1, \dots, N$ data points. For the main manuscript, these were extracted for aspect ratios larger than 0.8 from the previous work on in vitro infection assays⁷⁶ described in the previous Methods in Experimental Data. The fitted curve *Diam*(*t*) can be seen

in Fig. 2A, and the fitted parameters can be found in Supplementary Table S1. Also, it shows the parameter of the model fit for two further experimental settings: (i) described in the previous section (see Supplementary Fig. S1C), and ii) extracted from Alonso et al.,³¹ (Supplementary Fig. S1D). We performed the parameter estimation using the package *SciPy.optimize*⁷⁷ of the *SciPy 1.13.0* library in *Python 3.10*.

Modeling the uptake of conidia via an extended Malthus ODE model

In our approach, we assumed permanent contact between AECs and conidia. We model the uptake of conidia by type 2 AECs with an uptake rate r_{up}^{AEC2} , which corresponds to an uptake probability p_{up}^{AEC2} per time step. Based on the confrontation assays with type 2 AECs³⁵, which can be seen in Fig. 2C, we concluded that the uptake rate r_{up}^{AEC2} is increasing with time by the surface area increase over time *S*(*t*). Here, *S*(*t*) denotes the time-dependent mechanism that causes the increase in the uptake rate r_{up}^{AEC2} and by that the decrease in the number of free conidia *FreeCon*. Thus, we modeled the population of free conidia *FreeCon* with *FreeCon*(*t* = 0) = 1.0 (an initial population of 100%) with a Malthus ODE model (representing an exponential growth model) extended by the mechanism *S*:

$$\frac{d[FreeCon]}{dt} = -[FreeCon] \cdot r_{up0}^{AEC2} \cdot S(t) \quad (4)$$

A more detailed derivation of the extended Malthus ODE model from the normal Malthus ODE model is presented in Supplementary Results 1.4. We denote the uptake rate as $r_{up}^{AEC2}(t) := r_{up0}^{AEC2} \cdot S(t)$ that depends on the surface area increase over time *S*(*t*) and the parameter $r_{up0}^{AEC2} := r_{up}^{AEC2}(t = 0)$, representing the uptake rate at $t = 0$. We assume half the surface area of the conidium (modeled as a sphere) is in permanent contact with one type 2 AEC and *S*(*t*) to be describing the contact area over time relative to $t = 0$ min:

$$S(t) = \frac{2\pi \left(\frac{Diam(t)}{2} \right)^2}{2\pi \left(\frac{Diam(t=0)}{2} \right)^2} = \left(\frac{Diam(t)}{Diam(t=0)} \right)^2 = \left(\frac{[Diam] + D_{rest}^0}{D_{swell}^0 + D_{rest}^0} \right)^2 \quad (5)$$

By representing *S*(*t*) in by the means of [*Diam*], the term becomes time-independent and can be included in Eq. (5) as shown in Eq. (6). The resulting system of ODEs, including Eqs. (1), (4), and (5) models the population of free conidia *FreeCon*, linked to the conidial swelling and subsequent increasing contact area between conidia host cell (HC). Based on *FreeCon*, we can model the opposite conidia population, the percentage of conidia that was taken up by the respective host cells (HCs), e.g., type 1 or type 2 AECs or AMs, denoted as the uptake index *UI*. This is the actual model that we fit and is described by the *UI_{HC}* ODE Model as $UI_{HC}(t) = 1 - FreeCon(t)$. Minimizing the mean squared error *MSE*, as conducted in Methods Section, Eq. (3), of the extended Malthus ODE model to the data from infection assays with type 2 AECs, we were able to fit the model output to the data (see Fig. 2C and Supplementary Table S2). In addition, a cross-validation was conducted to validate the model's robustness and compare it to the normal Malthus ODE, as seen in Supplementary Results 1.2.

Extended hybrid agent-based model of the human alveolus

The previously developed virtual infection model of one human alveolus is a hybrid agent-based model (hABM) and was used in numerous studies to assess a to-scale infection scenario between the early immune reaction and the pathogenic fungus *A. fumigatus*^{13,30,58–60}. The hABM reproduces the anatomical and physiological spatiotemporal characteristics of one of the approximately 500 million human alveoli as a $\frac{3}{4}$ sphere on a cellular and molecular level. It encompasses both type 1 and type 2 AECs, along with pores of Kohn (PoKs) that facilitate air pressure, and cell and molecule exchange between neighboring alveoli. In the model, the proportional

surface coverage of type 1 (~ 95%) and type 2 (~ 5%) AECs is reflected through lung cell counts and alveolar measures taken from Stone et al. (1992)¹² calculated down to one alveolus. Thus, the initial condition for one stochastic simulation is given by the random placement of one conidium on type 1 or type 2 AEC and randomly placed type 2 AECs, PoKs, and AMs. After a concealment time of the conidium, the underlying AEC starts to secrete chemokines to attract the resident alveolar macrophages (AM). The AM follows the chemokine gradient through a biased persistent random walk, exhibiting chemotactic migration (see Supplementary Videos S1 and S2). This is based on the previously introduced diffusion of chemokines (Pollmächer et al.³⁹) that takes place on the inner surface of the alveolus which is modeled by partial differential equations and solved with the Euler scheme on discrete grid points (see Supplementary Video S1) approximating the 3/4 sphere of the alveolus^{59,78}. For the chemokine secretion, the optimal configuration of secretion rate s_{AEC} and diffusion coefficient D , of $s_{AEC}/D = 2.1 \times 10^3 \mu m^{-2}$, with $D = 20 \mu m^2 / min$ was applied, as found previously¹³. Further parameters were set to values extracted from literature or were screened in previous publications to which we refer here^{13,30,58–60}. Each infection scenario is simulated for $t_{max} = 8h$ with a time step of $\Delta t = 0.1$ min. Because of the amount of data per timestep, we write an output (the data points) only every 30 min. It is important to note that we consider the first six hours of infection before the moment when germination and hyphal growth are expected to set in.

In the current study, we extended the hABM to incorporate the uptake of conidia by AECs and AMs. While in previous studies, the detection time was studied, i.e. the first time point until an AM touched the conidium (compare with “Infection Score”), we here study the uptake time by AECs and AMs. For this, we fitted and implemented a time-dependent uptake mechanism (see Methods in Modeling the uptake of conidia via an extended Malthus ODE model), namely the uptake rate $r_{up}^{HC}(t) = r_{up0}^{HC} \cdot S(t)$ with $r_{up0}^{HC} := r_{up0}^{HC}(t = 0)$ of the of the respective HC for all HCs including type 1 and type 2 AECs and AMs described by a system of ODEs and included it in the hABM:

$$\frac{d[FreeCon]}{dt} = -[FreeCon] \cdot r_{up0}^{HC} \cdot \left(\frac{[Diam] + D_{rest}^0}{D_{swell}^0 + D_{rest}^0} \right)^2, \quad (6)$$

$$FreeCon(t = 0) = 1.0$$

$$\frac{d[Diam]}{dt} = r_{swell} \cdot [Diam_{swell}] \left(1 - \frac{[Diam_{swell}]}{C_{swell}} \right), \quad (7)$$

$$Diam_{swell}(t = 0) = D_{swell}^0$$

The presented ODE of increasing diameter is simultaneously solved, within each hABM simulation, using the Euler method⁷⁸ with the same time step of $\Delta t = 0.1$ min while the uptake is decided by the time-dependent (or diameter-dependent) uptake rates $r_{up}^{HC}(t) = r_{up0}^{HC} \cdot S(t)$, translating into the uptake probability $p_{up}^{HC}(t) = r_{up}^{HC}(t) \cdot \Delta t$ per time step, applied in the event of contact between HC and conidium. The values for r_{up0}^{AEC1} and r_{up0}^{AM} were screened while the $r_{up0}^{AEC2} = 0.00137 min^{-1}$ was fitted (see Methods in Modeling the uptake of conidia via an extended Malthus ODE model).

Input parameter and output measures for the extended hABM

To cover realistic infection scenarios, we screened over uptake rates of type 1 AECs r_{up0}^{AEC1} in the approximate regions of the fitted uptake rate of type 2 AECs. Moreover, we screened over up to 730-fold higher parameter regimes for uptake rates of AMs r_{up0}^{AM} compared to the fitted uptake rate of type 2 AECs r_{up0}^{AEC2} , because AECs are significantly less able to take up *A. fumigatus* than AMs, as indicated in in vivo and in vitro studies (see Supplementary Table S3). In addition, this exceeded values for the parameter regime of the AM uptake rates is supported by results provided in Supplementary Results 1.4 where we showed that estimated uptake rates of AMs from literature tend to be underestimated compared to uptake rates of AECs, due to a neglected AM migration time towards the conidium, in contrast to stationary AECs. Also, we screened over delayed onsets of chemokine

secretion $t_{s_{AEC}}$ by AEC. Depending on the timely recognition of a conidium by AECs on their surface, chemokines are released to attract AMs leading to chemotactic movements and directed immune responses⁶⁴. We hypothesized that the onset of chemokine secretion may depend on the state of conidial swelling during the first hours post-infection (see Supplementary Table S4). Consequently, we simulated infection scenarios assuming that the secretion of chemokines is triggered by a minor (3% after $t = 60$ min), medium (27% after $t = 120$ min), or substantial ($\geq 113\%$ after $t \geq 180$ min) swelling state of the conidium (see Fig. 2B). In addition, we also varied AM numbers and considered a low ($n_{AM} = 4$), average ($n_{AM} = 12$), and increased ($n_{AM} = 28$) presence of these immune cells¹³ simulating different states of the immune system.

As an output, we measure the proportion of simulations in which the conidium was taken up by (i) type 1 AECs, (ii) type 2 AECs, or (iii) AM after a time t . We call this measure the relative uptake index, denoted as $UI_{HC} \in [0, 1]$. In this regard, it is important to distinguish between the relative uptake index UI_{HC} that is calculated over the conidia that can be reached by the respective host cell and the absolute uptake index $UI_{HC}^* = w_{HC} UI_{HC}$ for a weight $w_{HC} \in [0, 1]$, that is calculated over all conidia. The weight w_{HC} describes the proportion of conidia that can be reached by the respective host cell and is used to derive the absolute uptake index from the relative uptake index. If the host cell can reach all conidia, e.g., AMs or AECs (type 1 & type 2), meaning $w_{HC} = 1.0$, then the relative uptake index is equal to the absolute uptake index, $UI_{HC}^* = UI_{HC}$. As combined measures, we consider the combined uptake by type 1 and type 2 AECs (UI_{AEC}), the overall or total uptake index (UI), and the uptake comparison (UC), denoting whether AMs or AECs take up more conidia. The weights $w_{AEC} = w_1 + w_2 = 1.0$, $w_{AM} = 1.0$, they are calculated as:

$$UI_{AEC} = w_1 UI_{AEC1} + w_2 UI_{AEC2}, \quad UI = w_{AEC} UI_{AEC} + w_{AM} UI_{AM}, \quad (8)$$

$$UC = w_{AEC} UI_{AEC} - w_{AM} UI_{AM}$$

To obtain the relative uptake contribution normalized to the overall uptake indexes (which can be lower than 100%), we calculate the uptake contribution per cell type as UI_{AEC}/UI for AECs and UI_{AM}/UI for AMs. To calculate error bars for each parameter configuration, we ran 10,000 simulations to guarantee statistical stability with 95% confidence intervals of $CI = UI_{HC} + / - 1.96 \cdot \sqrt{UI_{HC}(100 - UI_{HC})/n_{HC}}$, as obtained from the standard error of n_{HC} independent Bernoulli trials, while n_{HC} is the number of simulations accounting for the respective UI_{HC} . Overall parameter configurations, we ran about 10 million computer simulations (see Table 1). The hABM was implemented and extended in modern C++, and its code base is provided in the available code section. The stochastic simulations of our vectorized and highly parallelized hABM were conducted on an AMD EPYC 7742 64-core processor. One data point which is averaged from 10,000 simulations, took up to one hour. Using several machines with multiple processors, the total computation time for all simulations was around one month.

The surrogate infection model using a multilayer perceptron

In order to analyze the simulated parameter space systematically, we trained a surrogate infection model (SIM), which resembles the SIM in our previous study, which was referred to as MLP¹³. Here, we fitted a feedforward multilayer perceptron (MLP), which is a fully connected artificial neural network, on output values of the hABM to interpolate the parameter space without running the cost-intensive 10,000 hABM simulations per parameter configuration. The SIM allowed reducing computational costs for stochastic simulations via the hABM, while accurately predicting hABM simulation outcomes. Among other machine learning approaches, we chose the MLP for the SIM because it can be directly adapted to a changing number of input and output variables. In this case, the model $SIM : \mathbb{R}^5 \rightarrow [0, 1]^2$ consists of five input variables (r_{up0}^{AEC1} , r_{up0}^{AM} , $t_{s_{AEC}}$, n_{AM} , t) and two output variables (UI_{AEC} , UI_{AM}) whereby $UI_{AEC} \in [0, 1]$ summarizes the uptake proportion by type 1 and type 2 AECs together and $UI_{AM} \in [0, 1]$ the uptake

proportion by AMs. With these two outputs, the main measurements of uptake comparison ($UC = UI_{AEC} - UI_{AM}$) and uptake index ($UI = UI_{AEC} + UI_{AM}$) could be straightforwardly computed. We implemented the MLP with two hidden layers (21 and 11 neurons) and a logistic activation function. We fitted the SIM with a mean squared error of $MSE = 2.63 \cdot 10^{-5}$ (see Methods in Modeling the swelling of *A. fumigatus* conidia by a Verhulst ODE model) as a cost function. For the implementation of the MLP as a SIM and its optimization, we utilized the package *PyTorch 1.13 in Python 3.10*⁷⁹, which is provided in the available code.

Statistics and reproducibility

The results presented are reproducible within the statistic uncertainties using the given code⁸⁰ and data⁸¹ resources (see also code and data availability statement) and description of the models in the Methods. To reproduce the in silico simulation results with the hABM, the code can be downloaded, compiled, and run for the given parameter configurations in Table 1. With this, the provided raw data and resulting Fig. 3 can be reproduced. The error bars in Fig. 3 represent the 95% confidence interval of the stochastic computer simulations resulting from 10,000 simulations per parameter combination. The fit of the deterministic Verhulst ODE (diameter) and (extended) Malthus ODE (uptake) models shown in Fig. 2 can be reproduced using the provided code and the provided experimental data. The uncertainty bands shown in Fig. 2 represent the 95% confidence interval of the model predictions and were computed via a bootstrap method (see Supplementary Results 1.2). The surrogate infection model can be retrained and evaluated using the provided code enabling the reproduction of Figs. 5–7. The individual models were fit to (i) the experimental data, i.e., the ODE models, and (ii) the simulated data, i.e., the SIM, using the MSE as cost-function and the package *SciPy.optimize*⁷⁷ and the package *PyTorch 1.13 in Python 3.10*⁷⁹ respectively, that is also provided in the available code.

Reporting summary

Further information on research design is available in the Nature Portfolio Reporting Summary linked to this article.

Data availability

The raw simulation data from the hABM, the experimental data about uptake and diameter to which the ODE models have been fitted, and the Supplementary Videos can be accessed here https://asbdata.hki-jena.de/SafferEtAl2024_1 (<https://doi.org/10.5281/zenodo.14068066>).

Code availability

Any code regarding the derived ODE Models, the extended hybrid agent-based model (hABM), and the derived surrogate infection model (SIM) can be accessed here <https://github.com/applied-systems-biology/hABM-AlveolusModel-v2> (<https://doi.org/10.5281/zenodo.14056838>).

Received: 24 May 2024; Accepted: 22 November 2024;

Published online: 04 December 2024

References

- Gopallawa, I., Dehinwal, R., Bhatia, V., Gujar, V. & Chirmule, N. A four-part guide to lung immunology: Invasion, inflammation, immunity, and intervention. *Front. Immunol.* **14**, <https://doi.org/10.3389/fimmu.2023.1119564> (2023).
- Carlier, F. M., de Fays, C. & Pilette, C. Epithelial barrier dysfunction in chronic respiratory diseases. *Front. Physiol.* **12**, <https://doi.org/10.3389/fphys.2021.691227> (2021).
- Moraes, T. J., Chow, C. W. & Downey, G. P. *Clinical Respiratory Medicine*. (2012).
- Wang, S. & Hubmayr, R. D. Type I alveolar epithelial phenotype in primary culture. *Am. J. Respir. Cell Mol. Biol.* **44**, 692–699 (2011).
- Wang, Y. et al. Pulmonary alveolar type I cell population consists of two distinct subtypes that differ in cell fate. *Proc. Natl. Acad. Sci. USA* **115**, 2407–2412 (2018).
- Mason, R. J. Biology of alveolar type II cells. *Respirology* **11**, S12–S15 (2006).
- Bertuzzi, M., Hayes, G. E. & Bignell, E. M. Microbial uptake by the respiratory epithelium: Outcomes for host and pathogen. *FEMS Microbiol. Rev.* **43**, 145–161 (2019).
- Westphalen, K. et al. Sessile alveolar macrophages communicate with alveolar epithelium to modulate immunity. *Nature* **506**, 503–506 (2014).
- Bhattacharya, J. & Westphalen, K. Macrophage-epithelial interactions in pulmonary alveoli. *Semin. Immunopathol.* **38**, 461–469 (2016).
- O'Brien, A. D., Standiford, T. J., Christensen, P. J., Wilcoxon, S. E. & Paine, R. Chemotaxis of alveolar macrophages in response to signals derived from alveolar epithelial cells. *J. Lab. Clin. Med.* **131**, 417–424 (1998).
- Kannan, S. et al. Alveolar epithelial type II cells activate alveolar macrophages and mitigate *P. aeruginosa* infection. *PLoS ONE* **4**, <https://doi.org/10.1371/journal.pone.0004891> (2009).
- Stone, K. C., Mercer, R. R., Gehr, P., Stockstill, B. & Crapo, J. D. Allometric relationships of cell numbers and size in the mammalian lung. *Am. J. Respir. Cell Mol. Biol.* **6**, 235–243 (1992).
- Saffer, C., Timme, S., Rudolph, P. & Figge, M. T. Surrogate infection model predicts optimal alveolar macrophage number for clearance of *Aspergillus fumigatus* infections. *NPJ Syst. Biol. Appl.* **9**, 12 (2023).
- Ibrahim-Granet, O. et al. Phagocytosis and intracellular fate of *Aspergillus fumigatus* conidia in alveolar macrophages. *Infect. Immun.* **71**, 891–903 (2003).
- Neupane, A. S. et al. Patrolling alveolar macrophages conceal bacteria from the immune system to maintain homeostasis. *Cell* **183**, 1–16 (2020).
- Aberdein, J. D., Cole, J., Bewley, M. A., Marriott, H. M. & Dockrell, D. H. Alveolar macrophages in pulmonary host defence—the unrecognized role of apoptosis as a mechanism of intracellular bacterial killing. *Clin. Exp. Immunol.* **174**, 193–202 (2013).
- Joshi, N., Walter, J. M. & Misharin, A. V. Alveolar macrophages. *Cell Immunol.* **330**, 86–90 (2018).
- Whitsett, J. A. & Alenghat, T. Respiratory epithelial cells orchestrate pulmonary innate immunity. *Nat. Immunol.* **16**, 27–35 (2015).
- Dagenais, T. R. T. & Keller, N. P. Pathogenesis of *Aspergillus fumigatus* in invasive aspergillosis. *Clin. Microbiol. Rev.* **22**, 447–465 (2009).
- Latge, J. P., Chamilos, G. *Aspergillus fumigatus* and Aspergillosis in 2019. *Clin. Microbiol. Rev.* **30**, <https://doi.org/10.1128/cmr.00140-18> (2020).
- Taccone, F. S. et al. Epidemiology of invasive aspergillosis in critically ill patients: Clinical presentation, underlying conditions, and outcomes. *Crit. Care* **19**, 1–15 (2015).
- Arastehfar, A. et al. *Aspergillus fumigatus* and aspergillosis: From basics to clinics. *Stud. Mycol.* **100**, <https://doi.org/10.1016/j.simyco.2021.100115> (2021).
- WHO releases first-ever list of health-threatening fungi. <https://www.who.int/news/item/25-10-2022-who-releases-first-ever-list-of-health-threatening-fungi>.
- Fisher, M. C. & Denning, D. W. The WHO fungal priority pathogens list as a game-changer. *Nat. Rev. Microbiol.* **21**, 211–212 (2023).
- Parums, D. V. Editorial: The World Health Organization (WHO) Fungal Priority Pathogens List in Response to Emerging Fungal Pathogens During the COVID-19 Pandemic. *Med. Sci. Monit.* **28**, <https://doi.org/10.12659/msm.939088> (2022).
- Codina, R., Fox, R. W., Lockey, R. F., DeMarco, P. & Bagg, A. Typical levels of airborne fungal spores in houses without obvious moisture problems during a rainy season in Florida, USA. *J. Investig. Allergol. Clin. Immunol.* **18**, 156–162 (2008).
- Latge, J. P. The pathobiology of *Aspergillus fumigatus*. *Trends Microbiol.* **9**, 382–389 (2001).

28. Chai, L. Y. A., Netea, M. G., Vonk, A. G. & Kullberg, B. J. Fungal strategies for overcoming host innate immune response. *Med. Mycol.* **47**, 227–236 (2009).
29. Marcos, C. M. et al. Anti-immune strategies of pathogenic fungi. *Front. Cell. Infect. Microbiol.* **6**, <https://doi.org/10.3389/fcimb.2016.00142> (2016).
30. Blickensdorf, M., Timme, S. & Figge, M. T. Comparative assessment of aspergillosis by virtual infection modeling in murine and human lung. *Front. Immunol.* **10**, <https://doi.org/10.3389/fimmu.2019.00142> (2019).
31. Alonso, M. F., Bain, J. M., Erwig, L. P., Brown, A. J. P. & Gow, N. A. R. Fungal spore swelling and germination are restricted by the macrophage phagolysosome. *Fungal Biol.* **127**, 1291–1297 (2023).
32. Kwon-Chung, K. J. & Sugui, J. A. Aspergillus fumigatus—What makes the species a Ubiquitous human fungal pathogen? *PLoS Pathog.* **9**, 1–4 (2013).
33. Rhodes, J. C. Aspergillus fumigatus: Growth and virulence. *Med. Mycol.* **44**, 77–81 (2006).
34. Luo, Y. et al. Innate and Adaptive Immune Responses Induced by Aspergillus fumigatus Conidia and Hyphae. *Curr. Microbiol.* **80**, <https://doi.org/10.1007/s00284-022-03102-1> (2023).
35. Bertuzzi, M. et al. Epithelial uptake of Aspergillus fumigatus drives efficient fungal clearance in vivo and is aberrant in Chronic Obstructive Pulmonary Disease (COPD). Preprint at <https://doi.org/10.1101/2022.02.01.478664> (2022).
36. Bertuzzi, M. et al. Epithelial uptake leads to fungal killing in vivo and is aberrant in COPD-derived epithelial cells. *iScience* **27**, <https://doi.org/10.1016/j.isci.2024.109939> (2024).
37. Amin, S., Thywissen, A., Heinekamp, T., Peter, H. & Brakhage, A. A. Melanin dependent survival of Aspergillus fumigatus conidia in lung epithelial cells. *Int. J. Med. Microbiol.* **304**, 626–636 (2014).
38. Brakhage, A. A., Bruns, S., Thywissen, A., Zipfel, P. F. & Behnsen, J. Interaction of phagocytes with filamentous fungi. *Curr. Opin. Microbiol.* **13**, 409–415 (2010).
39. Luther, K. et al. Characterisation of the phagocytic uptake of Aspergillus fumigatus conidia by macrophages. *Microbes Infect.* **10**, 175–184 (2008).
40. Madan, T. et al. Binding of pulmonary surfactant proteins A and D to aspergillus fumigatus conidia enhances phagocytosis and killing by human neutrophils and alveolar macrophages. *Infect. Immun.* **65**, 3171–3179 (1997).
41. Ortiz, S. C., Pennington, K., Thomson, D. D. & Bertuzzi, M. Novel insights into aspergillus fumigatus pathogenesis and host response from state-of-the-art imaging of host–pathogen interactions during infection. *J. Fungi* **8**, <https://doi.org/10.3390/jof8030264> (2022).
42. Satora, L., Gawlikowski, T., Tański, A. & Formicki, K. Quest for breathing: proliferation of alveolar type 1 cells. *Histochem. Cell Biol.* **157**, 393–401 (2022).
43. Tavassoly, I., Goldfarb, J. & Iyengar, R. Systems biology primer: the basic methods and approaches. *Essays Biochem.* **62**, 487–500 (2018).
44. Medyukhina, A., Timme, S., Mokhtari, Z. & Figge, M. T. Image-based systems biology of infection. *Cytom. Part A* **87**, 462–470 (2015).
45. Ewald, J. et al. Dynamic optimization reveals alveolar epithelial cells as key mediators of host defense in invasive aspergillosis. *PLoS Comput. Biol.* **17**, 1–21 (2021).
46. Pollmächer, J. et al. Deciphering the counterplay of aspergillus fumigatus infection and host inflammation by evolutionary games on graphs. *Sci. Rep.* **6**, 1–15 (2016).
47. Dühring, S. et al. Modelling the host-pathogen interactions of macrophages and Candida albicans using Game Theory and dynamic optimization. *J. R. Soc. Interface* **14**, <https://doi.org/10.1098/rsif.2017.0095> (2017).
48. Tyc, K. M. et al. The game theory of Candida albicans colonization dynamics reveals host status-responsive gene expression. *BMC Syst. Biol.* **10**, <https://doi.org/10.1186/s12918-016-0268-1> (2016).
49. Tyc, K. M., Kühn, C., Wilson, D. & Klipp, E. Assessing the advantage of morphological changes in Candida albicans: A game theoretical study. *Front. Microbiol.* **5**, <https://doi.org/10.3389/fmicb.2014.00041> (2014).
50. Tille, A., Lehnert, T., Zipfel, P. F. & Figge, M. T. Quantification of factor H mediated self vs. non-self discrimination by mathematical Modeling. *Front. Immunol.* **11**, 1–13 (2020).
51. Hünninger, K. et al. A Virtual Infection Model Quantifies Innate Effector Mechanisms and Candida albicans Immune Escape in Human Blood. *PLoS Comput. Biol.* **10**, <https://doi.org/10.1371/journal.pcbi.1003479> (2014).
52. Lehnert, T. et al. Bottom-up modeling approach for the quantitative estimation of parameters in pathogen-host interactions. *Front. Microbiol.* **6**, 1–15 (2015).
53. Timme, S. et al. Quantitative simulations predict treatment strategies against fungal infections in virtual neutropenic patients. *Front. Immunol.* **9**, 1–14 (2018).
54. Tokarski, C. et al. Agent-based modeling approach of immune defense against spores of opportunistic human pathogenic fungi. *Front. Microbiol.* **3**, <https://doi.org/10.3389/fmicb.2012.00129> (2012).
55. Lehnert, T. et al. Comparative assessment of immune evasion mechanisms in human whole-blood infection assays by a systems biology approach. *PLoS ONE* **16**, <https://doi.org/10.1371/journal.pone.0249372> (2021).
56. Sreekantapuram, S. et al. Dynamic interplay of host and pathogens in an Avian Whole-Blood Model. *Front. Immunol.* **11**, 1–20 (2020).
57. Lehnert, T. & Figge, M. T. Dimensionality of motion and binding valency govern receptor-ligand kinetics as revealed by agent-based modeling. *Front. Immunol.* **8**, 1–14 (2017).
58. Blickensdorf, M., Timme, S. & Figge, M. T. Hybrid agent-based modeling of aspergillus fumigatus infection to quantitatively investigate the role of pores of Kohn in Human Alveoli. *Front. Microbiol.* **11**, 1–13 (2020).
59. Pollmächer, J. & Figge, M. T. Deciphering chemokine properties by a hybrid agent-based model of Aspergillus fumigatus infection in human alveoli. *Front. Microbiol.* **6**, 1–14 (2015).
60. Pollmächer, J. & Figge, M. T. Agent-based model of human alveoli predicts chemotactic signaling by epithelial cells during early Aspergillus fumigatus infection. *PLoS ONE* **9**, <https://doi.org/10.1371/journal.pone.0111630> (2014).
61. Philippe, B. et al. Killing of Aspergillus fumigatus by alveolar macrophages is mediated by reactive oxidant intermediates. *Infect. Immun.* **71**, 3034–3042 (2003).
62. Xia, D. et al. An adenoviral vector encoding full-length dectin-1 promotes aspergillus-induced innate immune response in macrophages. *Lung* **193**, 549–557 (2015).
63. Sobol, I. M. Sensitivity Estimates for Nonlinear Mathematical Models. *Mmce* **1**, 407–414 (1993).
64. Balloy, V. et al. Aspergillus fumigatus-induced interleukin-8 synthesis by respiratory epithelial cells is controlled by the phosphatidylinositol 3-kinase, p38 MAPK, and ERK1/2 pathways and not by the toll-like receptor-MyD88 pathway. *J. Biol. Chem.* **283**, 30513–30521 (2008).
65. Okaa, U. J. et al. Aspergillus fumigatus drives tissue damage via iterative assaults upon mucosal integrity and immune homeostasis. *Infect. Immun.* **91**, <https://doi.org/10.1128/iai.00333-22> (2023).
66. Bouyssi, A. et al. Characterization of lung inflammatory response to aspergillus fumigatus spores. *J. Fungi* **9**, <https://doi.org/10.3390/jof9060682> (2023).
67. Gresnigt, M. S. et al. Reducing hypoxia and inflammation during invasive pulmonary aspergillosis by targeting the Interleukin-1 receptor. *Sci. Rep.* **6**, 26490 (2016).

68. Wasylnka, J. A. & Moore, M. M. *Aspergillus fumigatus* conidia survive and germinate in acidic organelles of A549 epithelial cells. *J. Cell Sci.* **116**, 1579–1587 (2003).
69. Keizer, E. M. et al. Variation of virulence of five *Aspergillus fumigatus* isolates in four different infection models. *PLoS ONE* **16**, <https://doi.org/10.1371/journal.pone.0252948> (2021).
70. Bertuzzi, M. et al. On the lineage of *Aspergillus fumigatus* isolates in common laboratory use. *Med. Mycol.* **59**, 7–13 (2021).
71. Seidel, C. et al. Phagolysosomal survival enables non-lytic hyphal escape and ramification through lung epithelium During *Aspergillus fumigatus* Infection. *Front. Microbiol.* **11**, 1–13 (2020).
72. Kemp, S. J. et al. Immortalization of human alveolar epithelial cells to investigate nanoparticle uptake. *Am. J. Respir. Cell Mol. Biol.* **39**, 591–597 (2008).
73. Mosig, A. S. Organ-on-chip models: New opportunities for biomedical research. *Future Sci. OA* **3**, 2–4 (2017).
74. Hoang, T. N. M. et al. Invasive aspergillosis-on-chip: A quantitative treatment study of human *Aspergillus fumigatus* infection. *Biomaterials* **283**, 121420 (2022).
75. Deinhardt-Emmer, S. et al. Co-infection with *Staphylococcus aureus* after primary influenza virus infection leads to damage of the endothelium in a human alveolus-on-a-chip model. *Biofabrication* **12**, <https://doi.org/10.1088/1758-5090/ab7073> (2020).
76. Bertuzzi, M. & Howell, G. J. Single-cell analysis of fungal uptake in cultured Airway Epithelial Cells Using Differential Fluorescent Staining and Imaging Flow Cytometry. *Methods Mol. Biol.* **2260**, 83–109 (2021).
77. Virtanen, P. et al. SciPy 1.0: fundamental algorithms for scientific computing in Python. *Nat. Methods* **17**, 261–272 (2020).
78. Griffiths, D. F. & Higham, D. J. Euler's Method. 19–31 (2010).
79. Paszke, A. et al. PyTorch: An imperative style, high-performance deep learning library. *Adv. Neural Inf. Process Syst.* **32**, (2019).
80. Applied Systems Biology. Repo:applied-systems-biology/hABM-AlveolusModel-v2: Computer code: Hybrid agent-based model of one human alveolus (hABM). Zenodo. <https://doi.org/10.5281/zenodo.14056838>.
81. Saffer, C. et al. (2024). Raw simulation data of manuscript: Spatiotemporal modeling quantifies cellular contributions to uptake of *Aspergillus fumigatus* in the human lung. Zenodo <https://doi.org/10.5281/zenodo.14068066> (2024).

Acknowledgements

This work was supported by the German Research Foundation (DFG) through the CRC/TR 124 FungiNet with project number 210879364 (Project B4 to M.T.F.) and the excellence graduate school Jena School for Microbial Communication (JSMC). Furthermore, financial support was given by the German Federal Ministry of Education and Research within the funding program Photonics Research Germany, Project Leibniz Center for Photonics in Infection Research, Subproject LPI-BT3, contract number 13N15709. M.B. and S.O. are supported by the Medical Research Council (MRC New Investigator Research Grant MR/V031287/1 to M.B.).

Author contributions

M.T.F. conceived and designed this study. M.T.F. provided computational resources. Data processing, implementation, and application of the computational algorithm were done by C.S. C.S., S.T., S.O., M.B., and M.T.F. evaluated and analyzed the results of this study. C.S., S.T., and M.T.F. drafted the manuscript, and C.S., S.T., S.O., M.B., and M.T.F. revised the manuscript critically for important intellectual content and final approval of the version to be published. C.S., S.T., S.O., M.B., and M.T.F. agree to be accountable for all aspects of the work in ensuring that questions related to the accuracy or integrity of any part of the work are appropriately investigated and resolved.

Competing interests

The authors declare no competing interests.

Additional information

Supplementary information The online version contains supplementary material available at <https://doi.org/10.1038/s42003-024-07302-2>.

Correspondence and requests for materials should be addressed to Marc Thilo Figge.

Peer review information *Communications Biology* thanks the anonymous reviewers for their contribution to the peer review of this work. Primary Handling Editors: Aylin Bircan and Tobias Goris.

Reprints and permissions information is available at <http://www.nature.com/reprints>

Publisher's note Springer Nature remains neutral with regard to jurisdictional claims in published maps and institutional affiliations.

Open Access This article is licensed under a Creative Commons Attribution-NonCommercial-NoDerivatives 4.0 International License, which permits any non-commercial use, sharing, distribution and reproduction in any medium or format, as long as you give appropriate credit to the original author(s) and the source, provide a link to the Creative Commons licence, and indicate if you modified the licensed material. You do not have permission under this licence to share adapted material derived from this article or parts of it. The images or other third party material in this article are included in the article's Creative Commons licence, unless indicated otherwise in a credit line to the material. If material is not included in the article's Creative Commons licence and your intended use is not permitted by statutory regulation or exceeds the permitted use, you will need to obtain permission directly from the copyright holder. To view a copy of this licence, visit <http://creativecommons.org/licenses/by-nc-nd/4.0/>.

© The Author(s) 2024